Check for updates

JGR Solid Earth

RESEARCH ARTICLE
10.1029/2021JB022896

Rayleigh-Love Discrepancy Highlights Temporal Changes in Near-Surface Radial Anisotropy After the 2004 Great Sumatra Earthquake

W. Yu[1], T.-R. A. Song[2], J. Su[3], and J.-T. Lin[4]

[1]Institute of Earth Sciences, Academia Sinica, Nangang, Taiwan, [2]Department of Earth Sciences, University College London, London, UK, [3]Earth-Life Science Institute, Tokyo Institute of Technology, Meguro-ku, Japan, [4]Department of Earth Sciences, University of Oregon, Eugene, OR, USA

Key Points:

- We define "Rayleigh-Love discrepancy" as a stronger velocity reduction of Rayleigh wave than that of Love wave after the Sumatra Earthquake
- Rayleigh-Love discrepancy is inconsistent with a velocity change in isotropic media, but an increase in radial anisotropy near the surface
- Time-varying Rayleigh-Love discrepancy reflects changes in fluid-filled horizontal cracks under cyclic loading by successive earthquakes

Supporting Information:

Supporting Information may be found in the online version of this article.

Correspondence to:

W. Yu,
fgsyw@earth.sinica.edu.tw

Citation:

Yu, W., Song, T.-R. A., Su, J., & Lin, J.-T. (2021). Rayleigh-Love discrepancy highlights temporal changes in near-surface radial anisotropy after the 2004 Great Sumatra Earthquake. *Journal of Geophysical Research: Solid Earth*, *126*, e2021JB022896. https://doi.org/10.1029/2021JB022896

Received 26 JUL 2021
Accepted 29 NOV 2021

Author Contributions:

Conceptualization: W. Yu, T.-R. A. Song
Formal analysis: W. Yu, T.-R. A. Song, J. Su, J.-T. Lin
Funding acquisition: W. Yu, T.-R. A. Song
Investigation: W. Yu, T.-R. A. Song
Methodology: W. Yu, T.-R. A. Song
Software: W. Yu, J. Su, J.-T. Lin
Validation: W. Yu, T.-R. A. Song
Writing – original draft: W. Yu, T.-R. A. Song
Writing – review & editing: W. Yu, T.-R. A. Song, J. Su, J.-T. Lin

© 2021. American Geophysical Union. All Rights Reserved.

Abstract Strong ground motions from large earthquakes are capable of damaging near-surface sediments and promoting notable reductions in their seismic velocity structures. These velocity reductions can be monitored using either body waves or surface waves from repeatable seismic sources, such as repeating earthquakes (REs) or ambient seismic noise. Here, we compile a decade-long catalog of REs since the 2004 M_w 9.2 Sumatra Earthquake, and monitor the temporal velocity changes from Rayleigh waves (δV_{LR}) and Love waves (δV_{LQ}). We observe a δV_{LR} of −0.16% and $\delta V_{LR}/\delta V_{LQ}$ ratio of ~6, inconsistent with velocity reductions in isotropic media. To reconcile the observations, we carry out analyses of sensitivity kernels of surface waves in isotropic and vertical transversely isotropic (VTI) media and forward waveform modeling. The modeling reveals that the observed large $\delta V_{LR}/\delta V_{LQ}$ ratio can be explained by strong $d\beta_V$ (−4%) and weak $d\beta_H$ (−0.615%) reductions and an increase in radial anisotropy in the near surface. These changes are best explained by a 2% increase in crack density of aligned horizontal cracks in overpressured sediments near the compressive subduction zone forearc. Temporal variations of $\delta V_{LR}/\delta V_{LQ}$ ratios and radial anisotropy after consecutive great earthquakes are consistent with laboratory experiments under cyclic loading and unloading.

Plain Language Summary This study detects temporal changes in the wave speeds of long-period Rayleigh and Love waves after the 2004 Great Sumatra Earthquake, which were measured from repeating earthquakes. Seismic observations reveal that the Rayleigh-wave speed reduction is more than that of Love waves by a factor of 6. Love waves are much more sensitive to the *S*-wave speed of the shallow crust than Rayleigh waves in isotropic media (i.e., the *S*-wave speed is the same in all directions). One would therefore anticipate considerable Love-wave speed reduction if the *S*-wave speed reduction results from the near surface after great earthquakes. However, the observations indicate the opposite. The result of waveform modeling suggests that these unexpected observations can be suitably explained by an increase in radial anisotropy as a result of increasing fluid-filled horizontal cracks after great earthquakes.

1. Introduction

1.1. Review of Temporal Velocity Changes in Isotropic and Anisotropic Media

Repeatable seismic sources, including active sources (Niu et al., 2008; Vidale & Li, 2003), repeating earthquakes (REs) (K. H. Chen et al., 2015; Igarashi & Kato, 2021; Peng & Ben-Zion, 2006; Rubinstein et al., 2007; Uchida & Bürgmann, 2019), and ambient noise interferometry (Bensen et al., 2007; Brenguier et al., 2008; Lin et al., 2008; Takagi et al., 2012), are uniquely effective in probing changes in the seismic wave speed of the uppermost few kilometers of the crust. Previous analyses have shown substantial velocity changes (several percent) in the near-surface layer, likely induced by the strong ground motions of great earthquakes (Hobiger et al., 2016; Nakata & Snieder, 2011; Rubinstein et al., 2007; Wu et al., 2009; Yu et al., 2013a). In contrast, several studies have also provided evidence of subtle temporal velocity changes in the deep crust (Froment et al., 2013; Rivet et al., 2011; Yu et al., 2020), potentially associated with aseismic slip. Notably, the velocity reduction (δV) inferred from the body- and surface-wave measurements were discussed in isotropic media.

It is also understood that strong anisotropy, either in the form of azimuthal anisotropy (L. W. Chen et al., 2017; T. Y. Huang et al., 2015; Mordret et al., 2013) or radial anisotropy (Jeng et al., 2020; Naghavi et al., 2019; Shirzad et al., 2017; Tomar et al., 2017) have been detected in the near surface. Typically, azimuthal anisotropy

describes the azimuthal dependence of S-wave velocity (denoted as V_S or β) and particle motion within the horizontal plane, assuming a horizontal symmetry axis (i.e., horizontal transverse isotropy, abbreviated as "HTI") (Crampin, 1975). Shear-wave splitting, which measures the apparent fast polarization direction and the time delay between the fast and slow S waves traveling through anisotropic media (Crampin, 1981), has been widely used to probe earthquake-induced changes in azimuthal anisotropy near the surface (Cochran et al., 2003; Crampin et al., 1990; Liu et al., 2008; Peng & Ben-Zion, 2005; Savage et al., 1990). More recently, changes in azimuthal anisotropy were also determined by seismic interferometry (Durand et al., 2011; Nakata & Snieder, 2012; Saade et al., 2017, 2019; Sawazaki et al., 2018; Zuo et al., 2018). The interpretation of near-surface changes in azimuthal anisotropy often involves the presence of stress-induced cracks, where the S wave polarized parallel to the plane of the cracks travels at a higher velocity (Crampin, 1981). Since the orientation of cracks is subject to the background tectonic stress, changes in azimuthal anisotropy in the near surface after large earthquakes are related to variations in crack geometry, crack density (ε), and/or stress orientation.

Radial anisotropy is characterized by $\beta_V \neq \beta_H$, where β_V (or V_{SV}) and β_H (or V_{SH}) refer to the velocity of the horizontally propagating S waves polarized in the vertical and horizontal directions, respectively, in vertical transversely isotropic (VTI) media. Early observations of the "Rayleigh-Love discrepancy" typically referred to the fact that the phase (or group) velocity of Rayleigh and Love waves cannot be reconciled by a simple isotropic velocity model (Anderson, 1961; Babuska & Cara, 1991; Maupin & Cara, 1992), indicative of radial anisotropy. While crustal radial anisotropy was extensively investigated (Hu et al., 2020; H. Huang et al., 2010; Jaxybulatov et al., 2014; Moschetti et al., 2010; Shapiro et al., 2004), only a handful of studies investigated near-surface radial anisotropy (Jeng et al., 2020; Shirzad et al., 2017; Tomar et al., 2017). To our knowledge, no reports documented key observations indicative of changes in radial anisotropy in the near surface.

1.2. Summary of Earthquake-Induced Temporal Changes in δV in the Sumatra Subduction Zone

We have constructed REs catalog and used REs to detect time-varying δV since the 2004 Great Sumatra Earthquake recorded at the permanent seismic station PSI in Parapat, Sumatra, Indonesia, and several other stations (Figure 1) (Yu et al., 2013a, 2013b, 2020). It has been noted previously that temporal change in δV after the 2004 M_w 9.2 Sumatra and 2005 M_w 8.6 Nias earthquakes (Chlieh et al., 2007; Feng et al., 2015; Ishii et al., 2007; Konca et al., 2007) is likely associated with near-surface damage induced by strong ground motions. The latest work by Yu et al. (2020) (hereafter Y2020) also pointed out that temporal recovery in δV exhibits a bifurcation after late 2007 between the long-period (20-s period) Rayleigh wave (denoted as δV_{LR}) and high-frequency (HF, 0.8-s period) S coda wave (δV_S). The observed δV_S recorded at station PSI shows a steady and subtle recovery from 2005 to 2015, whereas the relatively large δV_{LR} displays an additional reduction after late 2007.

Y2020 showed that the bifurcation between δV_{LR} and δV_S after late 2007 and the observations of $\delta V_S << \delta V_{LR}$ can be reconciled by velocity changes in two zones. δV_{LR} after the 2004 and 2005 earthquakes can be explained by the "SF" models with a strong S-wave velocity reduction of $d\beta$ (or dV_S) $= -4\%$ confined to the uppermost 0.5–1.0 km of the crust. On the other hand, δV_S can be explained by a subtle $d\beta = -0.12\%$ over the 1–16 km depth range of the crust, corresponding to the "DL" models. A strong S-wave velocity reduction in the near surface can substantially alter δV_{LR}, but unable to reproduce the observed pattern of δV_S, whereas a subtle S-wave velocity reduction in the upper crust (the DL model) is necessary to account for the observed δV_S. Y2020 suggested that δV_S predominantly reflects post-seismic afterslip in the upper crust or/and viscous relaxation in the lower crust, whereas the strong δV_{LR} reflects damage confined to the near surface. Besides, a further reduction in δV_{LR} after late 2007 is consistent with re-damaging the subsurface sediments induced by strong ground motions of the 2007 M_w 8.4 and M_w 7.9 Bengkulu (Konca et al., 2008; Tsang et al., 2016) and 2008 M_w 7.3 Simeulue earthquakes (Table S1 in Supporting Information S1 for the event IDs of the major earthquakes).

Even though there were relatively few robust δV_{LQ} measurements (Yu et al., 2013a) (hereafter Y2013a), one puzzling observation is that δV_{LR} is 3–4 times larger than δV_{LQ} of Love wave recorded at PSI. Xu and Song (2009) investigated ambient noise cross-correlation between the seismic station pair PSI and CHTO in Chiang Mai, Thailand. Xu and Song (2009) also found a similar observation: a large delay time of +1.0 s for Rayleigh wave and a null delay time for Love wave after the 2004 and 2005 earthquakes. In a way, the observations of $\delta V_{LR} > \delta V_{LQ}$ are rather unexpected, since as elaborated in the later sections, Love wave is sensitive to the S-wave velocity in the shallower crust compared to Rayleigh wave in isotropic media. One would expect a strong δV_{LQ} or $\delta V_{LQ} > \delta V_{LR}$ if $d\beta$ is primarily confined in the near surface.

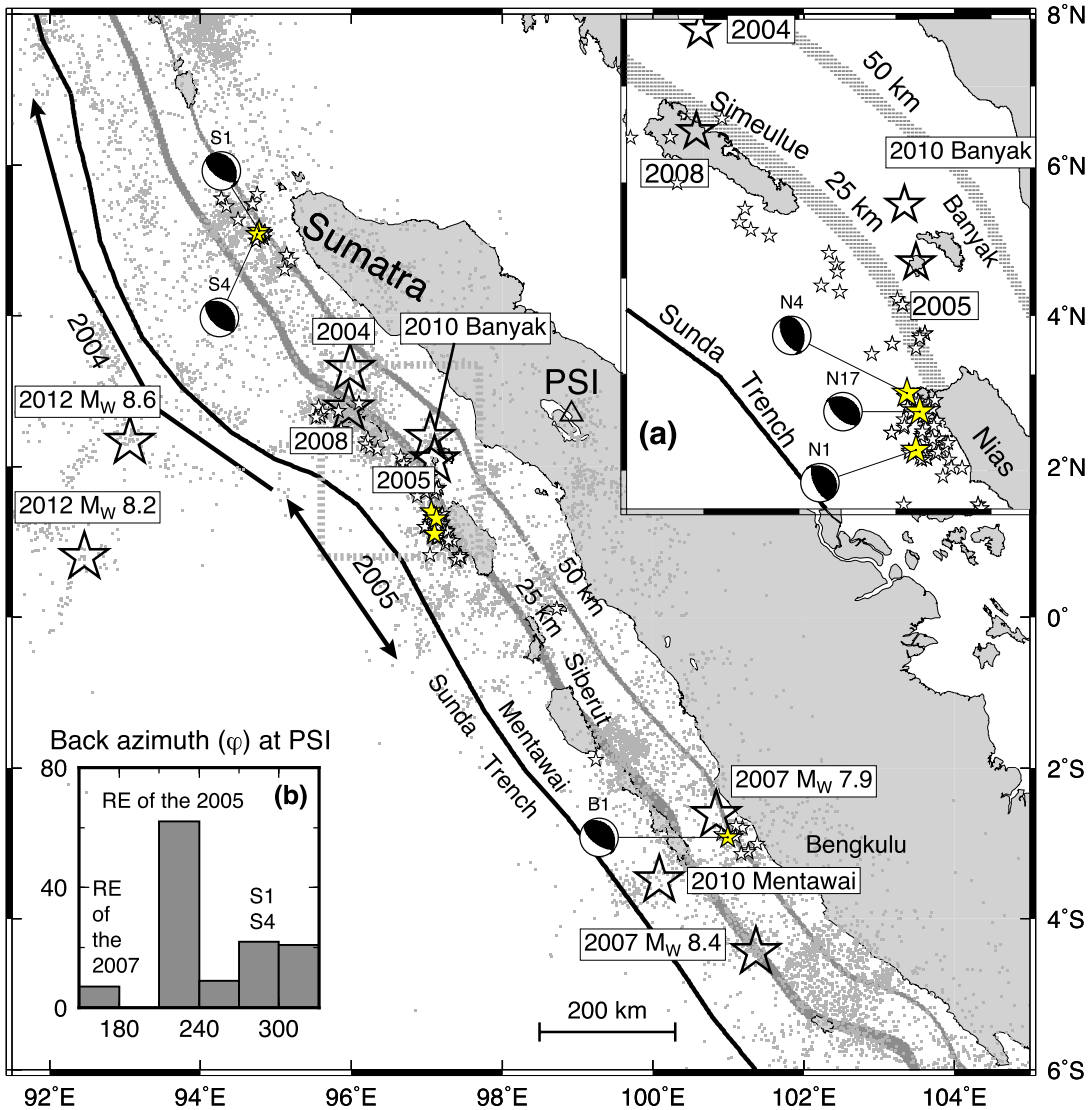

Figure 1. Regional seismicity map of the Sumatra Subduction Zone. The epicenters of several large earthquakes ($M_w \geq 7.3$) are shown as large open stars that are labeled with either their respective event IDs or M_w values (Table S1), repeating earthquake (RE) sequences are represented by small stars, and the background seismicity is represented by the gray dots. The black arrows show the rupture extent of the 2004 and 2005 earthquakes on the map. RE sequences for the relative locations (Table S2), and δV_{LR} and δV_{LQ} analyses are indicated by small yellow stars with the global centroid moment tensor (Ekström et al., 2012), whereas the REs with high cross-correlation (CC) coefficients and no further relocation analysis are indicated by small white stars; the source parameters of the latter are not provided. The solid black line indicates the Sunda trench (Bird, 2003), and the gray lines indicate the slab surface at 25 and 50 km depth in the Slab 1.0 model (Hayes et al., 2012). Seismograph station PSI is indicated by the open triangle. An enlarged map near the Nias, Banyak, and Simeulue Islands is displayed in the upper-right inset (a) to illustrate better the locations of the REs associated with the 2005 Nias Earthquake, with the gray dotted box indicating the region displayed in the main figure. The lower-left inset (b) displays the histogram of the back azimuth (φ) distribution of the δV_{LQ} data at station PSI.

The observations of $\delta V_{LR} > \delta V_{LQ}$ are inconsistent with $d\beta$ reductions in isotropic media, and we will demonstrate that such observations serve as a proxy for the change in radial anisotropy in the near surface. This study uses the term "Rayleigh-Love discrepancy" to indicate the observations of $\delta V_{LR} > \delta V_{LQ}$. In this report, we include additional 7 years of seismic data over the 2005–2015 time period to confirm the robustness of $\delta V_{LR} > \delta V_{LQ}$ (or large $\delta V_{LR}/\delta V_{LQ}$ ratios), and illustrate the time-varying δV_{LR} and δV_{LQ} observations. In the following sections, after outlining the method of RE detection and the procedure of δV measurements in Section 2, we first summarize the observations of δV_{LR} and δV_{LQ} over 2005–2015 in Section 3. In Section 4, we contrast the sensitivity kernels of Rayleigh wave and Love wave in isotropic and VTI media and elaborate on the scenarios where the observed high $\delta V_{LR}/\delta V_{LQ}$ ratio may be reconciled. These scenarios will serve as the basis in the forward modeling

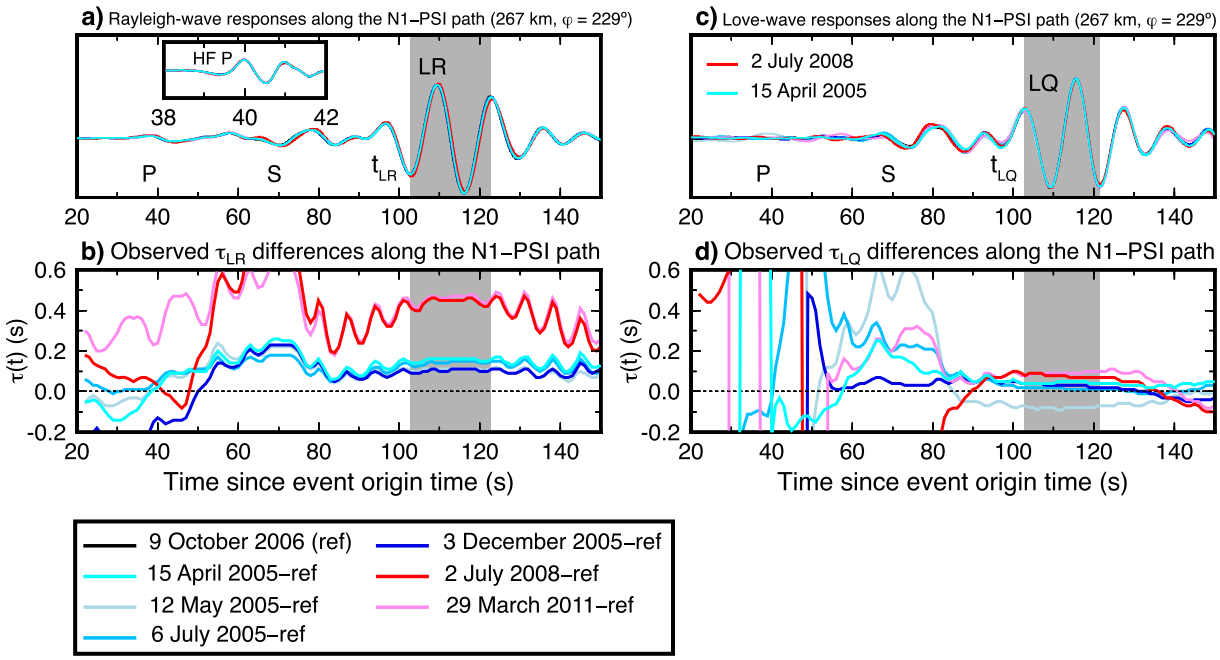

Figure 2. (a), (c) Waveforms and (b), (d) lag-time time series $\tau(t)$ for the N1 RE sequence recorded at station PSI. The vertical- and transverse-component data are shown for the long-period (10–33 s) (a), (b) Rayleigh (*LR*) and (c), (d) Love (*LQ*) waves, respectively. The epicentral distance (in km) and back azimuth (φ) are displayed in the titles. The high-frequency (HF; 0.5–2.0 s) *P*-wave onset is displayed in the inset in (a). The $\tau(t)$ values for the target event are computed relative to the reference event (black trace, October 9, 2006) and labeled "target event ID–ref." The blue and red traces are used to indicate the measured $\tau(t)$ and target events that occurred before and after the September 2007 Bengkulu earthquake sequence, respectively. The shaded regions correspond to the waveform segments with signal-to-noise ratios of ≥5 and CC coefficients of ≥0.9, which are used to compute δV (Equation 2). The unstable and oscillatory $\tau(t)$ values at the beginning are due to low signal-to-noise ratio values. The arrivals of *P*-, *S*-, Rayleigh-, and Love-wave arrivals are labeled as "P," "S," "LR" ("t_{LR}"), and "LQ" ("t_{LQ}"), respectively.

trials in Section 5, where we systematically validate the predictions from these models against the observations. Finally, we elaborate our preferred model in the context of the effective radial anisotropy in cracked media and briefly discuss the implications of change in crack geometry or/and crack density (ε) after great earthquakes in the subduction zone.

2. $\tau(t)$ and δV Measurements Between RE Pairs

The procedural details of the RE detection, relative location assessment within a given RE sequence, and the lag-time time series $\tau(t)$ and δV measurements have been discussed in the previous studies (Yu et al., 2013a, 2013b, 2020). Coda-wave interferometry (Poupinet et al., 1984; Snieder et al., 2002) is used to compute the lag-time time series $\tau(t)$ of the 20-s Rayleigh and Love waves at station PSI for a given RE sequence. $\tau_{LR}(t)$ and $\tau_{LQ}(t)$ are computed from the Rayleigh wave in the vertical component and the Love wave in the transverse component, respectively. The $\tau_{LR}(t)$ for the 20-s period Rayleigh waves can be expressed as follows:

$$\tau_{LR} = \left(t^{trg}_{20s\ \ LR} - t^{ref}_{20s\ \ LR}\right) - \left(t^{trg}_{HF\ \ P} - t^{ref}_{HF\ \ P}\right) \quad (1)$$

where t refers to the arrival time of the initial 0.8-s period (1.2 Hz) HF *P*-wave (subscript "HF *P*," inset of Figure 2a) and 20-s Rayleigh-wave (subscript "20s *LR*," Figure 2a) signals between the target (superscript "trg") and reference (superscript "ref") events of a given RE sequence. The relative velocity change for the Rayleigh wave (δV_{LR}) can be computed as follows:

$$\delta V_{LR} = -\frac{\bar{\tau}_{LR}}{t_{LR}} \quad (2)$$

where t_{LR} is the Rayleigh-wave arrival time and $\bar{\tau}_{LR}$ is the mean of the τ_{LR} values whose lapse time segments satisfy the thresholds of signal-to-noise ratios (SNR) ≥5 and cross-correlation (CC) coefficient ≥0.9. The $\tau_{LQ}(t)$ and

Table 1
List of the δV_{LR} and δV_{LQ} Data From RE Sequences and Similar Earthquake Pairs, and the δV Data Measured From Event Pairs With a Time Interval ≥0.5 years Included in KDE Analysis in Figure 3

	The number of δV from RE sequences	The number of δV from similar earthquake pairs	Total measurements	The number of δV with a time interval ≥0.5 years between target and reference events
δV_{LR}	84	508	592	422
δV_{LQ}	24	88	112	87

δV_{LQ} are computed in the same manner for Love waves. The details of $\tau_{LR}(t)$ and δV_{LR} uncertainties are presented in Text S1 in Supporting Information S1.

The δV_{LR} measurements are taken from Y2013a and Y2020, which include 84 measurements from 15 RE sequences and 508 measurements from similar earthquake pairs that are too small to have a sufficient number of stations for relocation, but with high quality (SNR ≥ 5) and highly correlated waveforms (CC ≥ 0.9). On the other hand, the δV_{LQ} measurements are primarily acquired in this report, including 24 new measurements from six RE sequences and 88 new measurements from similar earthquake pairs that are too small to have a sufficient number of stations for relocation, but with high quality (SNR ≥ 5) and highly correlated waveforms (CC ≥ 0.9) (Table 1). The new data set is an approximately sevenfold increase in the number of measurements that were analyzed in the previous study (Figure 3c of Y2013a). Examples of the relocation results of the six RE sequences and their source parameters are presented in Figure S1 and Table S2 in Supporting Information S1. Rayleigh and Love waveforms at station PSI and their corresponding $\tau_{LR}(t)$ and $\tau_{LQ}(t)$ for the six RE sequences are displayed in Figures 2 and S2–S6 in Supporting Information S1. In total, we acquired 592 δV_{LR} and 112 δV_{LQ} measurements from the waveforms recorded at station PSI (Table 1).

We note that for RE sequences associated with the 2004 Sumatra or 2005 Nias great earthquakes, the reference event is chosen as the last event before September 2007. On the other hand, we mostly choose the latest event as the reference event for REs associated with the September 12, 2007 M_w 8.4 and M_w 7.9 Bengkulu earthquakes (Table S2 and Figure S6 in Supporting Information S1). These choices allow us to highlight the additional increase in τ_{LR} induced by the 2007 Bengkulu earthquakes (Konca et al., 2008; Tsang et al., 2016) and the 2008 M_w 7.3 Simeulue earthquake (i.e., red traces in Figures 2b and S2b–S5b in Supporting Information S1, see also Section 3).

3. Observations of Large $\delta V_{LR}/\delta V_{LQ}$ Ratios After the 2004 Sumatra Earthquake

Many of the observed $\delta V_{LR}/\delta V_{LQ}$ ratios are in the ~4–6 range after the 2004 and 2005 great earthquakes (Chlieh et al., 2007; Feng et al., 2015; Hsu et al., 2006), and they increase slightly after the 2007 (Konca et al., 2008; Tsang et al., 2016) and 2008 earthquakes. We use δV in the probability density analysis and a kernel density estimation (abbreviated as "KDE") (Parzen, 1962) to investigate the δV_{LR} and δV_{LQ} distributions and establish the consistency and robustness of the observed δV_{LR} and δV_{LQ} values. The KDE is a representation of the probability density function $\hat{f}_h(x)$, and can be formulated as follows:

$$\hat{f}_h(x) = \frac{1}{n}\sum_{i=1}^{n} K\left(\frac{x - x_i}{h}\right) \tag{3}$$

where x_i is the ith δV value for a sample size n, h is the bandwidth value that controls the smoothness of the resultant probability density curve, and $K(x_i, h)$ is the kernel, which is expressed by the Gaussian function:

$$K(x_i, h) = \frac{1}{h\sqrt{2\pi}} \exp\left(-\frac{1}{2}\left(\frac{x - x_i}{h}\right)^2\right) \tag{4}$$

The peaks correspond to the maximum likelihood values for each set of δV values.

To ensure the robustness of the KDE analysis, the measurements made by event pairs separated by a time interval longer than 0.5 years are retained, including 422 δV_{LR} and 87 δV_{LQ} measurements (Table 1, Figures 3a and 3b). We use the timing of the September 2007 Bengkulu earthquake sequence to divide the δV values into two groups, before (blue curve, Group 1) and after the 2007 earthquakes (red curve, Group 2). The δV data in Groups 1 and 2 indicate those whose target events occurred before and after the September 2007 earthquakes, respectively. In general, the δV data in Group 1 mostly correspond to the recovery stage after the 2004/2005 great earthquakes, whereas the δV data in Group 2 correspond to the stage of an additional velocity reduction as a result of the 2007/2008 earthquakes. This division allows us to inspect the impact of subsequent earthquakes on changes in material properties. The peak δV_{LR} value decreases from −0.16% (Group 1) to −0.25% (Group 2, Figure 3a),

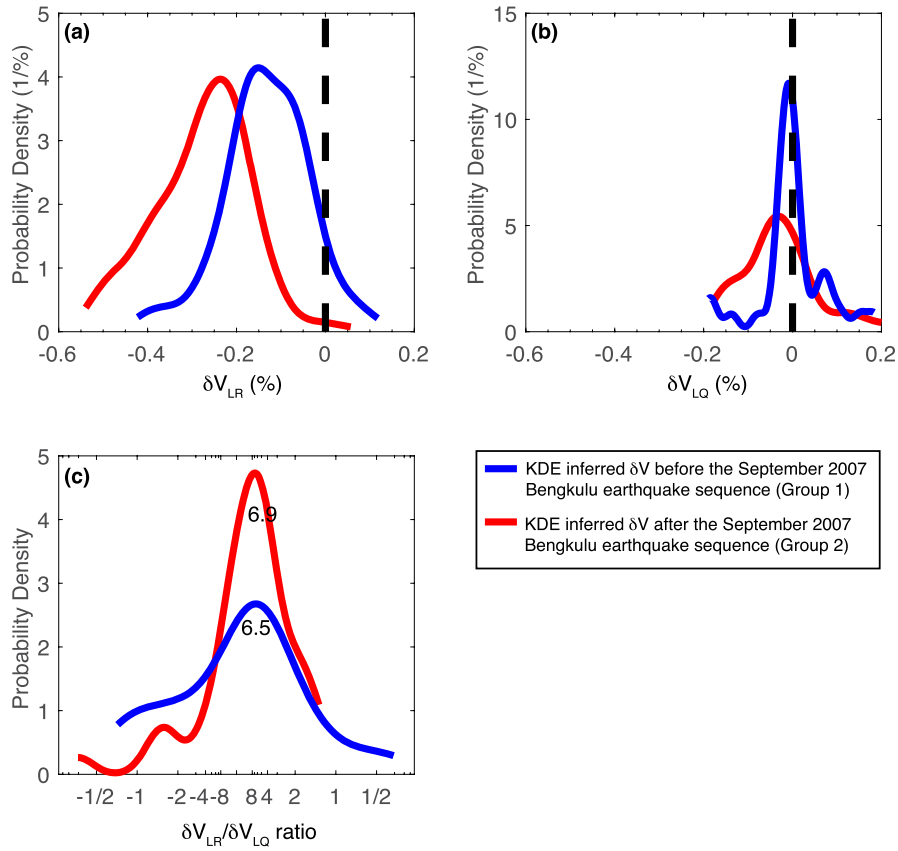

Figure 3. The kernel density estimation (KDE) inferred probability densities for the observed (a) δV_{LR}, (b) δV_{LQ}, and (c) $\delta V_{LR}/\delta V_{LQ}$ ratio distributions, which were measured from REs that have been relocated (Table S2) and those possess high CC coefficients, and calculated via Equations 3 and 4. The KDE-inferred δV before (Group 1) and after (Group 2) the September 2007 Bengkulu earthquake sequence are indicated by the blue and red curves, respectively. In (a), (b), the probability densities are defined in units of 1/%. In (c), the probability density of $\delta V_{LR}/\delta V_{LQ}$ ratio is presented in the functional form of $\cot^{-1}(x)$, where $x = \delta V_{LR}/\delta V_{LQ}$. Therefore, the peak corresponding to $\delta V_{LR}/\delta V_{LQ}$ ratio $= \infty$ is located in the center of the x-axis.

whereas the peak δV_{LQ} value also decreases from −0.008% (Group 1) to −0.027% (Group 2, Figure 3b). These observations indicate an additional velocity reduction after the 2007 earthquakes. The peak $\delta V_{LR}/\delta V_{LQ}$ ratios are 6.5 and 6.9 for Groups 1 and 2, respectively (Figure 3c). We also perform the same KDE analysis against data from RE sequences (Figure S7 in Supporting Information S1) and similar earthquake pairs (Figure S8 in Supporting Information S1), respectively. The results remain very similar. Furthermore, we do not find systematic differences in $\delta V_{LR}/\delta V_{LQ}$ ratios against the locations of REs (REs of the 2005 vs. REs of the 2004; Figures 2 and S1–S5 in Supporting Information S1). Note also the back azimuth (φ) of the station PSI against the recorded REs is in the range of ∼160–300°, suggesting that such a large $\delta V_{LR}/\delta V_{LQ}$ ratios can be consistently observed over a ∼140° azimuthal swath (inset (b) of Figure 1). In the following section, we contrast the sensitivity kernels of Rayleigh wave and Love wave in isotropic and VTI media to illustrate that change in anisotropy in VTI media can be consistent with the observed large $\delta V_{LR}/\delta V_{LQ}$ ratios.

4. Rayleigh Wave and Love Wave Sensitivity Kernels in Isotropic and VTI Media

4.1. Sensitivity Kernels in Isotropic Media

First, we compute the sensitivity kernels (partial derivatives) in isotropic media. The sensitivity kernels of surface wave phase-velocity $\frac{\alpha}{c}\left[\frac{\partial c}{\partial \alpha}\right]_{\omega}$ and $\frac{\beta}{c}\left[\frac{\partial c}{\partial \beta}\right]_{\omega}$ in isotropic media are computed using the DISPER80 code (Saito, 1988; Takeuchi & Saito, 1972), where α and β denote the P-wave and S-wave velocity, respectively, c is the phase velocity, and ω is the angular frequency. The kernels $\frac{\alpha}{c}\left[\frac{\partial c}{\partial \alpha}\right]_{\omega}$ and $\frac{\beta}{c}\left[\frac{\partial c}{\partial \beta}\right]_{\omega}$ are denoted as $K(\alpha)$ and $K(\beta)$, respectively.

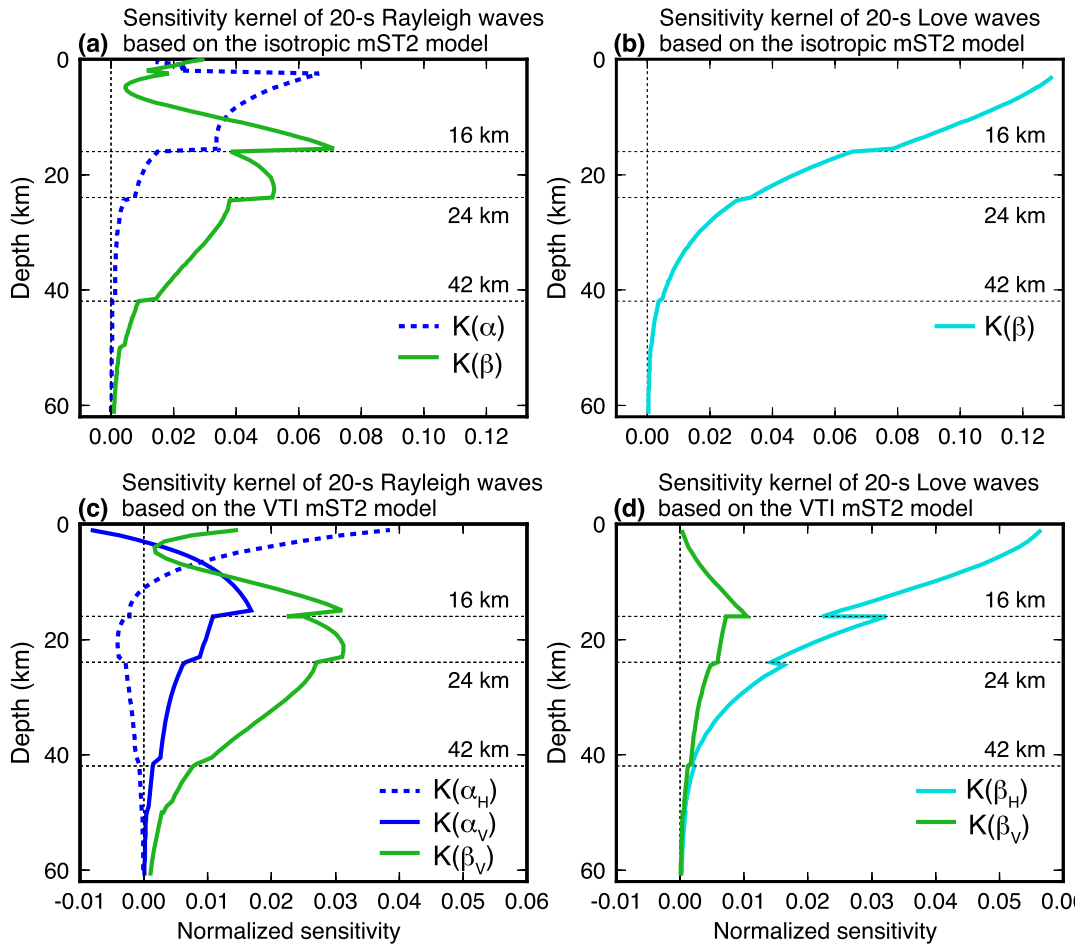

Figure 4. Sensitivity kernels of the 20-s (a) Rayleigh and (b) Love waves with respect to α and β in isotropic media, which are denoted as $K(\alpha)$ (dotted blue) and $K(\beta)$ (green for Rayleigh, light-blue for Love), respectively. Sensitivity kernels of the 20-s (c) Rayleigh waves with respect to α_H ($K(\alpha_H)$, dotted blue), α_V ($K(\alpha_V)$, solid blue), and β_V ($K(\beta_V)$, green) in VTI media and (d) Love waves with respect to β_H ($K(\beta_H)$, light-blue) and β_V ($K(\beta_V)$, green) in VTI media (Saito, 1988; Takeuchi & Saito, 1972); each sensitivity kernel is defined in the presentation of η_κ (Kawakatsu, 2016b). The horizontal lines on each plot indicate 16, 24, and 42 km depth.

These kernels are computed against the isotropic velocity model mST2, which includes the regional velocity model ST2 (Lange et al., 2010) in the upper 50 km and VTI PREM (Dziewonski & Anderson, 1981) over the 50–220 km depth range (Figure S9 and Table S3 in Supporting Information S1). The ST2 model is derived from regional *P*-wave and *S*- wave traveltime data sampling the forearc and the Sumatra Island. Synthetic seismograms from the direct solution method (DSM) (Kawai et al., 2006) based on the VTI mST2 velocity model are generally consistent with the observed Rayleigh waveforms (Figure S10 in Supporting Information S1).

The sensitivity kernels of the 20-s Rayleigh and Love waves based on the isotropic velocity model mST2 exhibit the following characteristics: (a) The Love-wave kernel $K(\beta)$ decreases considerably from the surface with depth (light-blue curve, Figure 4b). (b) The Rayleigh-wave kernel $K(\beta)$ increases from its minimum at 5 km depth to its maximum at 16 km depth (green curve, Figure 4a). The Rayleigh-wave kernel $K(\beta)$ is approximately 10 times smaller than the Love-wave kernel $K(\beta)$ at the surface (green curve in Figure 4a vs. light-blue curve in Figure 4b). (c) The Rayleigh-wave kernel $K(\alpha)$ increases from the surface to the peak at 2.5 km depth and decreases with depth (dotted blue curve, Figure 4a). The characteristics of these kernels confirm the notion that, the near-surface $d\beta$ velocity reductions in isotropic media, as derived from Y2020, will result in $\delta V_{LR} < \delta V_{LQ}$, inconsistent with the observations of large $\delta V_{LR}/\delta V_{LQ}$ ratios.

4.2. Sensitivity Kernels in VTI Media

We examine the sensitivity kernels in VTI media, which has one of the simplest anisotropy symmetry with five independent elastic constants, A, C, N, L, and F. A and C are related to the phase velocity of horizontally and vertically propagating P-waves, respectively, whereas N and L are related to the phase velocity of a horizontally propagating S wave polarized in the horizontal and vertical directions, respectively, where

$$\alpha_H = \sqrt{\frac{A}{\rho}} \quad \alpha_V = \sqrt{\frac{C}{\rho}} \quad \beta_H = \sqrt{\frac{N}{\rho}} \quad \beta_V = \sqrt{\frac{L}{\rho}} \tag{5}$$

and ρ refers to the density. A fifth parameter η is introduced to characterize the incidence angle dependence of body waves (Anderson, 1961; Takeuchi & Saito, 1972), and defined as

$$\eta = \frac{F}{(A - 2L)} \tag{6}$$

In the case of VTI, the strength of P-wave radial anisotropy ϕ and S-wave radial anisotropy ξ can be defined as

$$\phi = \frac{\alpha_H^2}{\alpha_V^2} \quad \xi = \frac{\beta_H^2}{\beta_V^2} \tag{7}$$

A new fifth parameter η_κ for describing vertical transverse isotropy is introduced in several recent studies (Kawakatsu, 2016a, 2016b; Kawakatsu et al., 2015), and η_κ is defined as

$$\eta_\kappa = \frac{F + L}{(A - L)^{1/2}(C - L)^{1/2}} \tag{8}$$

It has been shown the new parameter η_κ to be advantageous in greatly reducing the trade-off between α_V and η (Kawakatsu, 2016a). The comparisons between η_κ and η adopted for sensitivity-kernel computations are discussed in Text S2 and Figure S11 in Supporting Information S1. The sensitivity kernels of the surface wave phase-velocity c with respect to α_H, α_V, β_H, and β_V are expressed as $\frac{\alpha_H}{c}\left[\frac{\partial c}{\partial \alpha_H}\right]_\omega$, $\frac{\alpha_V}{c}\left[\frac{\partial c}{\partial \alpha_V}\right]_\omega$, $\frac{\beta_H}{c}\left[\frac{\partial c}{\partial \beta_H}\right]_\omega$, and $\frac{\beta_V}{c}\left[\frac{\partial c}{\partial \beta_V}\right]_\omega$, respectively. We abbreviate the expressions of sensitivity kernels as $K(\alpha_H)$, $K(\alpha_V)$, $K(\beta_H)$, and $K(\beta_V)$, respectively. The sensitivity kernels in VTI media are computed using the modified DISPER80 code (Saito, 1988; Takeuchi & Saito, 1972) in the presentation of η_κ, following Equation 3 of Kawakatsu (2016b). We have benchmarked $K(\alpha_H)$, $K(\alpha_V)$, and $K(\beta_V)$ of the fundamental mode of 30-s Rayleigh wave based on the VTI PREM model, and they are identical to those presented in Figures 1a and 1d of Kawakatsu (2016b).

The sensitivity kernels of the 20-s Rayleigh and Love waves based on the VTI mST2 velocity model exhibit the following additional characteristics. (a) The Rayleigh-wave kernel $K(\beta_V)$ is smaller than the Love-wave kernel $K(\beta_H)$ by a factor of 3.6 at the surface in VTI media (green curve in Figure 4c vs. light-blue curve in Figure 4d). (b) The Rayleigh-wave kernel $K(\alpha_H)$ is larger than the Rayleigh-wave kernel $K(\alpha_V)$ by a factor of four near the surface (dotted blue curve vs. solid blue curve in Figure 4c). In a way, Rayleigh waves are sensitive to the vertically polarized S-wave velocity (β_V), the horizontally propagating P-wave velocity (α_H), and, to a lesser degree, the vertically propagating P-wave velocity (α_V), whereas Love waves are sensitive to the horizontally polarized S-wave velocity (β_H) in VTI media.

The comparisons of sensitivity kernels in isotropic and VTI media lead to several scenarios that may reproduce large $\delta V_{LR}/\delta V_{LQ}$ ratios: (I) a notable $d\alpha_H$ reduction or $d\alpha_H > d\alpha_V$ in the near surface; (II) a notable $d\beta_V$ reduction or $d\beta_V > d\beta_H$ in the near surface; and (III) $d\beta_V \geq d\beta_H$ below 20 km depth of the crust. Note that scenarios (I) and (II) also indicate an increase in the strength of both P-wave radial anisotropy ϕ and S-wave radial anisotropy ξ in the near surface.

5. Forward Modeling δV_{LR} and δV_{LQ} via the DSM Synthetics in VTI Media

Following the scenarios (I)–(III) discussed in Section 4, we use the forward modeling approach and systematically explore these scenarios and validate the predictions from a number of candidate models against the observations. In particular, we demonstrate that this approach offers quantitative estimates of the size and depth extent of

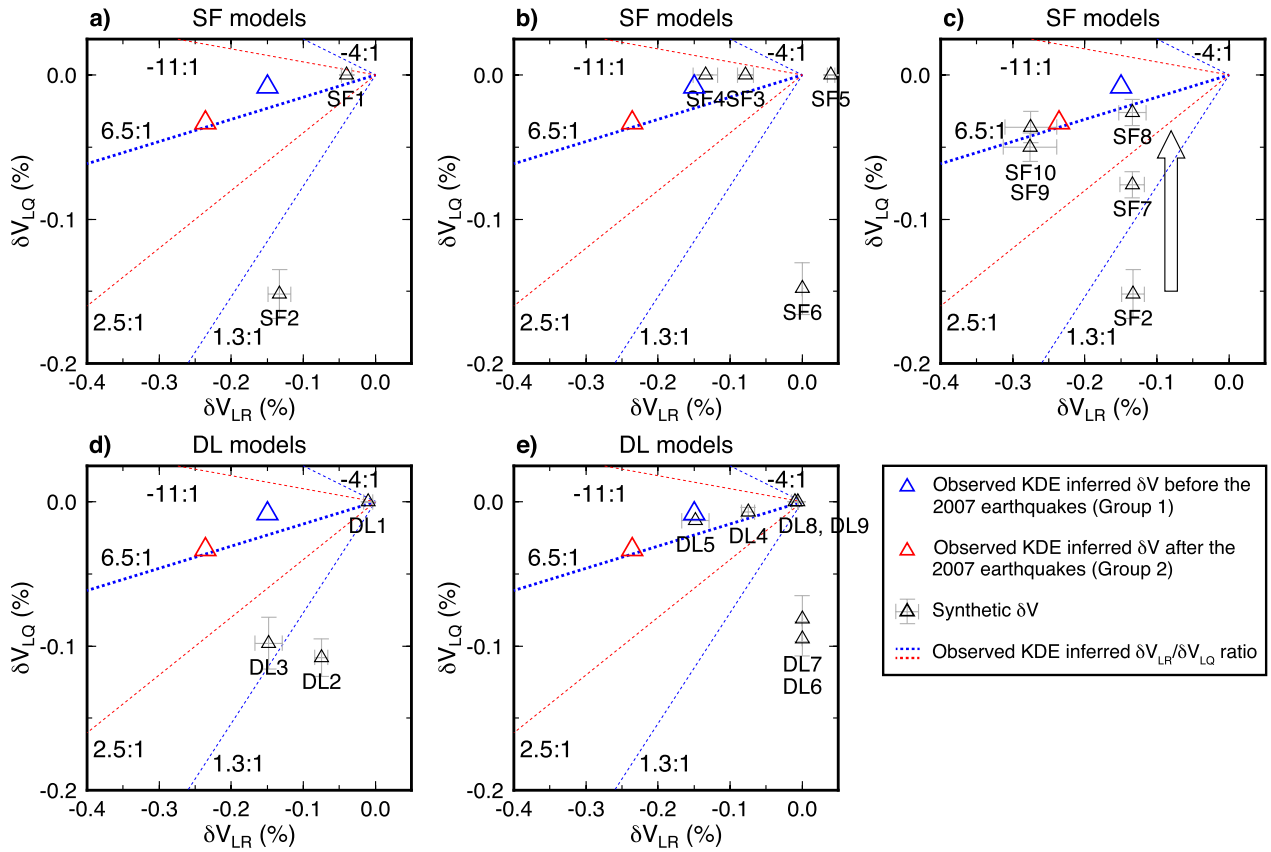

Figure 5. Synthetic δV_{LR} (x-axis) versus δV_{LQ} (y-axis) values (black triangles) based on (a, b, c) SF, and (d), (e) DL perturbed models superimposed on the observed KDE-inferred peak $\delta V_{LR}/\delta V_{LQ}$ ratio of 6.5 (thick-dotted blue line) and $\pm 1\sigma$ standard deviation (thin-dotted red/blue lines) and δV values (large blue/red triangles). Blue and red colors indicate the peak $\delta V_{LR}/\delta V_{LQ}$ ratio and δV measured from the observations in Groups 1 and 2, respectively (same as Figure 3). One σ of the peak $\delta V_{LR}/\delta V_{LQ}$ ratio in Group 1 is in the range of −4.0–1.3, denoted as −4:1 and 1.3:1, whereas 1σ of the peak $\delta V_{LR}/\delta V_{LQ}$ ratio in Group 2 is in the range of −11:1 and 2.5:1. The vertical arrow in (c) indicates the trend of the $\delta V_{LR}/\delta V_{LQ}$ ratio as increasing the $d\beta_V/d\beta_H$ ratio.

velocity perturbation in line with the models discussed in Y2020. Here synthetic seismograms are computed via the DSM in VTI media with accuracy up to 2 Hz (Kawai et al., 2006). We have modified the DSM and used Equation 8 to assign the elastic constant F for a given η_κ. The moment-tensor source mechanism of the RE sequence is acquired from the global centroid moment tensor (Ekström et al., 2012). The representative source-receiver geometry between the cluster N1 and the station PSI was considered in the calculations for all tested models.

Synthetic waveforms from the perturbed models and the reference model VTI mST2 are used to obtain synthetic $\tau(t)$ following the same processing steps as the observed waveforms. Synthetic δV_{LR} (or δV_{LQ}) values are computed from τ_{LR} (or τ_{LQ}) using Equation 2, and they are compared against the observed KDE-inferred peak $\delta V_{LR}/\delta V_{LQ}$ ratio (Figure 5) to discuss suitable candidate models. The candidate models are categorized based on the two-layer model discussed in Y2020, where relatively strong velocity changes occur in the near surface (i.e., 0–1 km, SF model) and weak velocity changes in the deep layer (i.e., 1–16 km or 16–24.4 km, DL model). The aim of the forward modeling approach is to explore several end-member models that can reproduce the key observation of large $\delta V_{LR}/\delta V_{LQ}$ ratios and reconcile $\delta V_S << \delta V_{LR}$. These end-member models include changes in $d\alpha_H$, $d\alpha_V$, $d\beta_H$, and $d\beta_V$ and the ratio of $d\alpha_V/d\alpha_H$ and $d\beta_V/d\beta_H$ over different depth extents (Table 2).

5.1. Synthetic $\delta V_{LR}/\delta V_{LQ}$ Ratios Based on Strong $d\alpha$ and $d\beta$ Perturbations Confined to the Surface (SF Models)

In the SF models, the velocity perturbations are confined to the uppermost 1 km of the surface. The SF1 model with P-wave velocity reductions of $d\alpha_H = d\alpha_V = -2\%$ (SF1) yields a δV_{LR} of −0.04% and δV_{LQ} of 0%, respectively (SF1, Figure 5a). The SF2 model with S-wave velocity reductions of $d\beta_H = d\beta_V = -4\%$ predicts a δV_{LR} of

Table 2
List of Perturbed Models Used to Compute the Direct Solution Method (DSM) (Kawai et al., 2006) Synthetic Seismograms, and the Associated Parameters That Were Modified to Perturb the VTI mST2 Reference Velocity Model

Model ID	Parameter perturbations in the VTI mST2 reference velocity model
SF1	$d\alpha_H = -2\%$ and $d\alpha_V = -2\%$ ($d\alpha_V/d\alpha_H = 1$) over the 0–1 km depth range (Surface denoted as SF)
SF2	$d\beta_H = -4\%$ and $d\beta_V = -4\%$ ($d\beta_V/d\beta_H = 1$) over the 0–1 km depth range
SF3	$d\alpha_H = -2\%$ over the 0–1 km depth range
SF4	$d\beta_V = -4\%$ over the 0–1 km depth range
SF5	$d\alpha_V = -2\%$ over the 0–1 km depth range
SF6	$d\beta_H = -4\%$ over the 0–1 km depth range
SF7	$d\beta_H = -2\%$ and $d\beta_V = -4\%$ ($d\beta_V/d\beta_H = 2$) over the 0–1 km depth range
SF8	$d\beta_H = -0.615\%$ and $d\beta_V = -4\%$ ($d\beta_V/d\beta_H = 6.5$) over the 0–1 km depth range
SF9	$d\beta_H = -1.23\%$ and $d\beta_V = -8\%$ ($d\beta_V/d\beta_H = 6.5$) over the 0–1 km depth range
SF10	$d\beta_H = -0.8\%$ and $d\beta_V = -8\%$ ($d\beta_V/d\beta_H = 10$) over the 0–1 km depth range
DL1	$d\alpha_H = -0.08\%$ and $d\alpha_V = -0.08\%$ ($d\alpha_V/d\alpha_H = 1$) over the 1–16 km depth range (Deep Layer, denoted as DL)
DL2	$d\beta_H = -0.16\%$ and $d\beta_V = -0.16\%$ ($d\beta_V/d\beta_H = 1$) over the 1–16 km depth range
DL3	$d\beta_H = -0.75\%$ and $d\beta_V = -0.75\%$ ($d\beta_V/d\beta_H = 1$) over the 16–24.4 km depth range
DL4	$d\beta_V = -0.16\%$ over the 1–16 km depth range
DL5	$d\beta_V = -0.75\%$ over the 16–24.4 km depth range
DL6	$d\beta_H = -0.16\%$ over the 1–16 km depth range
DL7	$d\beta_H = -0.75\%$ over the 16–24.4 km depth range
DL8	$d\alpha_H = -0.08\%$ over the 1–16 km depth range
DL9	$d\alpha_V = -0.08\%$ over the 1–16 km depth range
SCK1	Crack density (ε) = 2.0% and AR = 1 for spherical cracks, where the crack aspect ratio AR is defined as the ratio of the in-plane direction to the symmetry-axis direction, which outputs $d\alpha_H = -2.27\%$, $d\alpha_V = -2.25\%$, $d\beta_H = -1.86\%$, and $d\beta_V = -1.86\%$ over the 0–1 km depth range ($d\alpha_V/d\alpha_H = 1.0$, $d\beta_V/d\beta_H = 1.0$)
HCK2	$\varepsilon = 2.0\%$ and AR = 10 for horizontal cracks, where AR is defined as the ratio of the in-plane direction (horizontal axis) to the symmetry-axis direction (vertical axis) for horizontal cracks, which outputs $d\alpha_H = -2.72\%$, $d\alpha_V = -8.92\%$, $d\beta_H = -1.13\%$, and $d\beta_V = -5.76\%$ over the 0–1 km depth range ($d\alpha_V/d\alpha_H = 3.3$, $d\beta_V/d\beta_H = 5.1$)
HCK3	$\varepsilon = 2.0\%$ and AR = 30 for horizontal cracks (AR is defined in the same manner as the model HCK2), which outputs $d\alpha_H = -3.62\%$, $d\alpha_V = -13.34\%$, $d\beta_H = -1.05\%$, and $d\beta_V = -13.50\%$ over the 0–1 km depth range ($d\alpha_V/d\alpha_H = 3.7$, $d\beta_V/d\beta_H = 12.9$)
HCK4	$\varepsilon = 2.0\%$ and AR = 100 for horizontal cracks (AR is defined in the same manner as the model HCK2), which outputs $d\alpha_H = -4.21\%$, $d\alpha_V = -16.12\%$, $d\beta_H = -1.02\%$, and $d\beta_V = -30.34\%$ over the 0–1 km depth range ($d\alpha_V/d\alpha_H = 3.8$, $d\beta_V/d\beta_H = 29.7$)
HCK5	$\varepsilon = 4.0\%$ and AR = 10 for horizontal cracks (AR is defined in the same manner as the model HCK2), which outputs $d\alpha_H = -4.98\%$, $d\alpha_V = -15.96\%$, $d\beta_H = -2.26\%$, and $d\beta_V = -10.81\%$ over the 0–1 km depth range ($d\alpha_V/d\alpha_H = 3.2$, $d\beta_V/d\beta_H = 4.8$)
VCK6	$\varepsilon = 2.0\%$ and AR = 10 for vertical cracks, where AR is defined as the ratio of the in-plane direction (vertical axis) to the symmetry-axis direction (horizontal axis) for vertical cracks, which outputs $d\alpha_H = -8.92\%$, $d\alpha_V = -2.72\%$, $d\beta_H = -5.76\%$, and $d\beta_V = -5.76\%$ over the 0–1 km depth range ($d\alpha_V/d\alpha_H = 0.3$, $d\beta_V/d\beta_H = 1.0$)
VCK7	$\varepsilon = 0.5\%$ and AR = 30 for vertical cracks (AR is defined in the same manner as the model VCK6), which outputs $d\alpha_H = -3.89\%$, $d\alpha_V = -1.05\%$, $d\beta_H = -3.90\%$, and $d\beta_V = -3.90\%$ over the 0–1 km depth range ($d\alpha_V/d\alpha_H = 0.3$, $d\beta_V/d\beta_H = 1.0$)

Table 2
Continued

Model ID	Parameter perturbations in the VTI mST2 reference velocity model
VCK8	ε = 1.0% and AR = 30 for vertical cracks (AR is defined in the same manner as the model VCK6), which outputs $d\alpha_H = -7.36\%$, $d\alpha_V = -1.99\%$, $d\beta_H = -7.41\%$, and $d\beta_V = -7.41\%$ over the 0–1 km depth range ($d\alpha_V/d\alpha_H = 0.3$, $d\beta_V/d\beta_H = 1.0$)
VCK9	ε = 2.0% and AR = 30 for vertical cracks (AR is defined in the same manner as the model VCK6), which outputs $d\alpha_H = -13.34\%$, $d\alpha_V = -3.62\%$, $d\beta_H = -13.50\%$, and $d\beta_V = -13.50\%$ over the 0–1 km depth range ($d\alpha_V/d\alpha_H = 0.3$, $d\beta_V/d\beta_H = 1.0$)

Note. Perturbations of $d\alpha_H$, $d\alpha_V$, $d\beta_H$, and $d\beta_V$ for the SCK1–VCK9 cracked-solids models were computed using the Tandon and Weng (1984) formulations to determine the effective elastic moduli of fluid-filled inclusions using defined ε, AR, and orientation inputs. For cracked-solids (CK) model IDs, initials "S," "H," and "V" refer to spherical, horizontal, and vertical cracks, respectively.

−0.13% and a δV_{LQ} of −0.15%, respectively. Furthermore, the synthetic δV_{LQ} value is greater than the range of observations (SF2, Figure 5a). These two examples are consistent with the inferences from the sensitivity kernels in isotropic media, and they highlight the necessity to impose changes in velocity anisotropy in VTI media.

As noted in Section 4, Rayleigh waves are primarily sensitive to α_H and β_V, and less sensitive to α_V, whereas Love waves are sensitive to β_H near the surface in VTI media. $d\alpha_H = -2\%$ (SF3) and $d\beta_V = -4\%$ (SF4, Figure 5b) are able to reproduce the observed δV_{LR}, δV_{LQ}, and $\delta V_{LR}/\delta V_{LQ}$ ratio in Group 1 within ±1σ. $d\alpha_V = -2\%$ (SF5) and $d\beta_H = -4\%$ (SF6, Figure 5b) perturbations produce either a small, positive δV_{LR}, or large δV_{LQ}, respectively, and these models do not reproduce the observed $\delta V_{LR}/\delta V_{LQ}$ ratio.

It is conceivable that an increase in $d\beta_V/d\beta_H$ ratio for perturbations confined to the surface can amplify the $\delta V_{LR}/\delta V_{LQ}$ ratios effectively. As shown in Figure 5c, when the $d\beta_V/d\beta_H$ ratio increases from 1 (SF2) to 2 (SF7) or 6.5 (SF8), the synthetic $\delta V_{LR}/\delta V_{LQ}$ ratio increases from 0.9 to 1.8 or 5.5 for a fixed $d\beta_V = -4\%$. The models SF9 and SF10 include a stronger $d\beta_V$ of −8% and $d\beta_V/d\beta_H = 6.5$ and 10, respectively. These two models predict a δV_{LR} of −0.28% and $\delta V_{LR}/\delta V_{LQ}$ ratios of 5.5 and 7.7, consistent with the observed amplified δV_{LR} in Group 2.

5.2. Synthetic $\delta V_{LR}/\delta V_{LQ}$ Ratios Based on Subtle $d\alpha$ and $d\beta$ Perturbations in the Deep Layer of the Bulk Crust (DL Models)

Alternatively, we consider candidate models where small velocity changes are embedded in the deep layer of the depth range of 1–16 km or 16–24.4 km. The DL1 model with *P*-wave velocity reductions of $d\alpha_H = d\alpha_V = -0.08\%$ over the 1–16 km depth range produces δV_{LR} of ∼0% (DL1, Figure 5d), whereas the DL2 model with *S*-wave velocity reductions of $d\beta_H = d\beta_V = -0.16\%$ over the 1–16 km depth range produces a large δV_{LQ} value and a small $\delta V_{LR}/\delta V_{LQ}$ ratio (DL2, Figure 5d). Neither DL1 nor DL2 reconciles the observations. Similarly, the DL3 model with *S*-wave velocity reductions of $d\beta_H = d\beta_V = -0.75\%$ over the depth range of 16–24.4 km (DL3, Figure 5d) is unable to reproduce the observed large $\delta V_{LR}/\delta V_{LQ}$ ratios neither.

However, only when $d\beta_V$ is assigned in the deep layer, it produces a null δV_{LQ} and a large $\delta V_{LR}/\delta V_{LQ}$ ratio comparable to the observations (DL4 and DL5, Figure 5e). The model DL4, including a smaller $d\beta_V$ over the depth range of 1–16 km to explain the observed HF δV_S, predicts a slightly lower value than the observed peak δV_{LR} value, whereas the DL5 model includes a stronger $d\beta_V$ over the 16–24.4 km depth range can reproduce the peak δV_{LR} in Group 1 (Figure 5e). Finally, we test end-member models with perturbations of $d\beta_H$, $d\alpha_H$, or $d\alpha_V$ in the deep layer, but they do not reproduce the observed $\delta V_{LR}/\delta V_{LQ}$ ratio. Specifically, $d\beta_H$ in the deep layer produces a large δV_{LQ} and a small $\delta V_{LR}/\delta V_{LQ}$ ratio (DL6 and DL7, Figure 5e); $d\alpha_H$ (DL8) or $d\alpha_V$ (DL9) in the deep layer produce a $\delta V_{LR} \approx 0\%$ (Figure 5e).

In summary, the large $\delta V_{LR}/\delta V_{LQ}$ ratios observed in the data can be reproduced by the scenarios as stated previously: (I) a notable $d\alpha_H$ or $d\alpha_H >> d\alpha_V$ confined to the surface (SF3, Figure 5b), (II) a notable $d\beta_V$ or $d\beta_V/d\beta_H$ ratio ≥6.5 confined to the surface (SF4, Figure 5b, and SF8–SF10, Figure 5c), and (III) a notable $d\beta_V$ or $d\beta_V >> d\beta_H$ in the deep layer of the crust (DL5, Figure 5e).

5.3. Validating Scenarios (I)−(III) Against the Observations of $\delta V_S << \delta V_{LR}$

As documented in Y2020 and summarized in the previous sections, the bifurcation between δV_{LR} and δV_S after late 2007 can be reconciled by velocity changes in two zones. δV_{LR} after the 2004 and 2005 earthquakes can be explained by a strong S-wave velocity reduction of $d\beta = -4\%$ confined to the uppermost 0.5–1.0 km of the crust. δV_S can be explained by a subtle $d\beta \approx -0.1\%$ over the 1–16 km depth in the deep layer. To validate the successful end-member models discussed in Sections 5.1 and 5.2, it is critical to examine if the scenarios (I)−(III) can also reconcile the observations of $\delta V_S << \delta V_{LR}$. Since the scenarios (I) and (II) only invoke perturbations in the uppermost 1 km near the surface, Y2020 have demonstrated that velocity changes near the surface cannot reproduce the observed pattern of δV_S (Figure 12a of Y2020).

In the case of scenario (III), the model DL5 ($d\beta_V = -0.75\%$ at 16–24.4 km depth) can indeed produce a large $\delta V_{LR}/\delta V_{LQ}$ ratio (Figure 5e). However, the magnitude of $d\beta_V$ in the model DL5 is 1 order of magnitude larger than those discussed in Y2020 where $d\beta \approx -0.1\%$ over the 1–16 km depth. To validate scenario (III), we implement the finite difference method to compute the HF coda wavefield (detailed in Y2020) and assign the model FD-DL5 with a perturbation $d\beta = -0.55\%$ and root mean square perturbations of 25% over the same depth range as the model DL5 (Table S4 and Text S3 in Supporting Information S1). While the model FD-DL5 produces a good fit to the observed peak δV_{LR} value in Group 1, however, it results in δV_S over −2%, 10 times larger than the observations (Figure S12 in Supporting Information S1). Consequently, we conclude that scenario (III) is unlikely, and the large $\delta V_{LR}/\delta V_{LQ}$ ratios are predominantly contributed by either $d\beta_V > d\beta_H$ (scenario (II)) or $d\alpha_H > d\alpha_V$ (scenario (I)) confined to the surface.

6. Discussion

6.1. The Effective VTI Media of Fluid-Filled Cracked Solids

It has been frequently documented that velocity changes in the upper crust likely reflect changes in crack density (ε) (O'Connell & Budiansky, 1974). However, if the cracks are preferentially aligned, depending on crack geometry, one also expects changes in seismic anisotropy (Crampin, 1987; Crampin et al., 1990). For example, it has been shown that increasing ε of horizontal cracks produces $d\alpha_V > d\alpha_H$ and $d\beta_V > d\beta_H$ (Anderson et al., 1974). While both scenarios (I) and (II) can produce large $\delta V_{LR}/\delta V_{LQ}$ ratios, they imply opposing crack orientation or/and geometry. In the framework of fluid-filled cracked media, we evaluate the effective anisotropy against changes in ε, crack aspect ratio (AR), and orientation to distinguish scenario (I) from (II).

Following Tandon and Weng (1984), the crack aspect ratio (AR) can be defined as the ratio of the in-plane direction to the symmetry-axis direction. When AR = 1, spherical cracks do not possess any velocity anisotropy. For horizontal cracks, the in-plane direction and symmetry axis correspond to the horizontal and vertical axes, respectively. When AR >> 1, horizontal smarty-shape cracks possess a slow symmetry axis along the vertical axis, resulting in VTI anisotropy. On the other hand, when such horizontal smarty cracks are rotated vertically, they possess a slow symmetry axis along the horizontal axis, resulting in horizontal transversely isotropic (HTI) anisotropy. In this case, as the aligned cracks are sampled from diverse directions by Rayleigh and Love waves (inset (b) of Figure 1), we compute azimuthally averaged effective anisotropy (Montagner & Nataf, 1986) against ε, AR, and crack orientation.

We use the formulations of Tandon and Weng (1984) to compute the effective elastic constants (A, C, N, L, and F) and $d\alpha_H$, $d\alpha_V$, $d\beta_H$, and $d\beta_V$ of fluid-filled cracked solids. We set $\alpha = 4.4795$ km/s, $\beta = 2.24$ km/s, and $\rho = 2.6$ g/cm^3 for the crack-free solids in the uppermost 1 km in the mST2 model (Table S3 in Supporting Information S1). For crack-filled media, we define $\alpha = 1.45$ km/s, $\beta = 0$ km/s, and $\rho = 0.997$ g/cm^3 for the fluid inclusions. $d\alpha_H$, $d\alpha_V$, $d\beta_H$, and $d\beta_V$ based on given ε, AR, and crack orientation are implemented to the DSM to compute synthetic waveforms (models SCK1−VCK9 in Table 2). The synthetics based on the cracked-solids model are processed against those based on the VTI mST2 reference model (i.e., crack-free) to retain δV_{LR}, δV_{LQ}, and $\delta V_{LR}/\delta V_{LQ}$ ratios.

For horizontal cracks, increasing the AR from 1 (SCK1) to 10 (HCK2) to 30 (HCK3) to 100 (HCK4) with a fixed $\varepsilon = 2\%$ increases the $d\alpha_V/d\alpha_H$ and $d\beta_V/d\beta_H$ ratios progressively, equivalent to increasing the P-wave radial anisotropy ϕ and S-wave radial anisotropy ξ. Since ξ is stronger than ϕ due to changes of AR, as a consequence, the δV_{LR} and $\delta V_{LR}/\delta V_{LQ}$ ratios increase (Figure 6a). With a fixed AR = 10, increasing crack densities from 2%

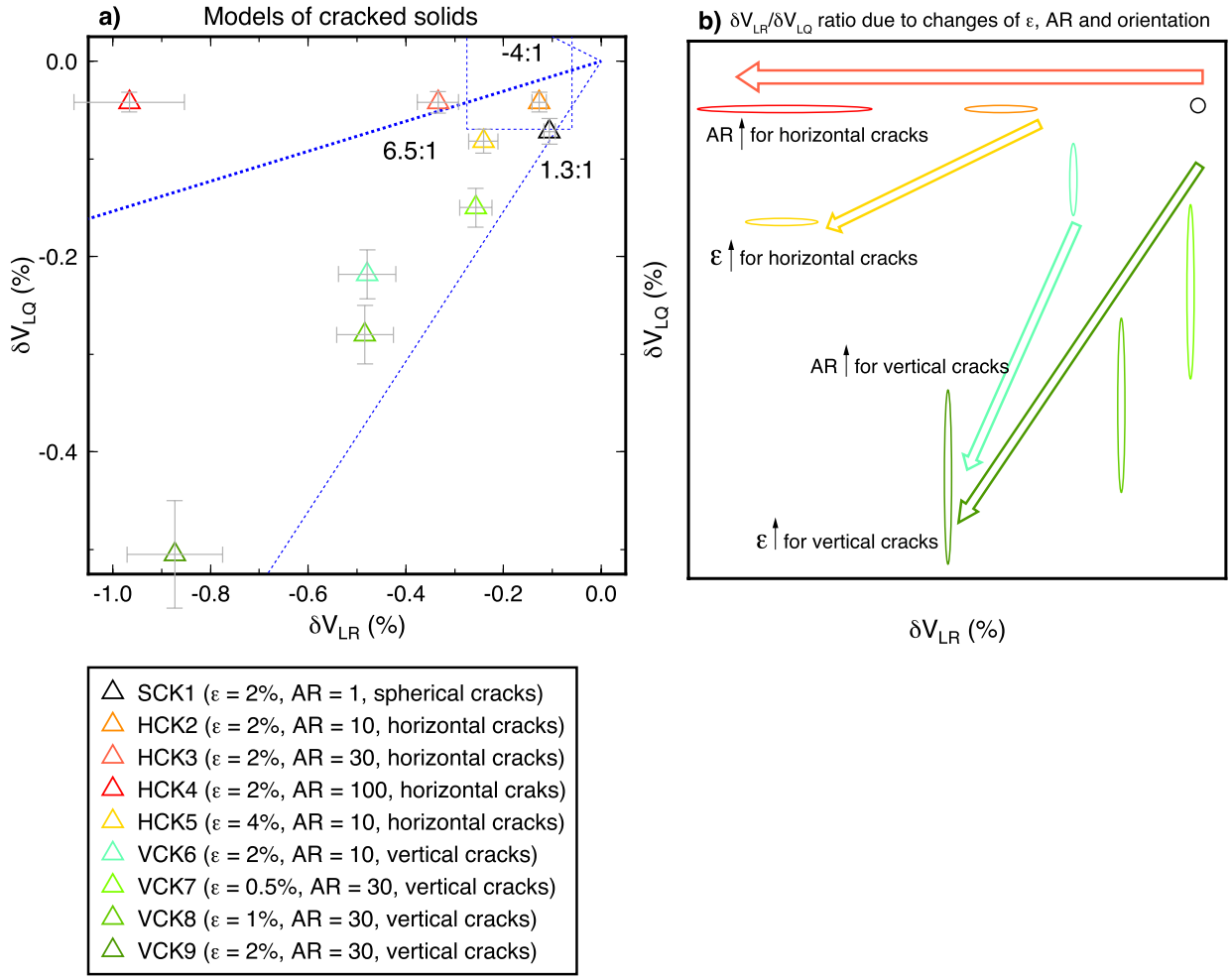

Figure 6. Similar to Figure 5, but for the cracked-solids models. Colors are used to distinguish models with crack density (ε), AR (defined as the crack aspect ratio of the in-plane direction to the symmetry-axis direction), and crack orientation. The text identifier follows the format: cracked-solids model ID (ε, AR, and crack orientation that is labeled as "spherical/horizontal/vertical cracks"). The thin-dotted blue box indicates $\pm 1\sigma$ of the observed KDE-inferred δV_{LR} and δV_{LQ} values in Group 1. Crack geometry and orientation of the tested models are represented as the proxy in (b). The horizontal red arrow indicates the trend of the $\delta V_{LR}/\delta V_{LQ}$ ratio as a result of increasing the AR from 1 (SCK1) to 10 (HCK2), 30 (HCK3), and 100 (HCK4) with a fixed $\varepsilon = 2\%$ for horizontal cracks. The yellow arrow indicates the effect of increasing the ε from 2% (HCK2) to 4% (HCK5) with a fixed AR = 10 for horizontal cracks. The dark-green arrow indicates the trend of the $\delta V_{LR}/\delta V_{LQ}$ ratio as increasing the ε from 0.5% (VCK7) to 1% (VCK8) and 2% (VCK9) with a fixed AR = 30 for vertical cracks. The cyan arrow indicates the effect of increasing the AR from 10 (VCK6) to 30 (VCK9) with a fixed $\varepsilon = 2\%$ for vertical cracks.

(HCK2) to 4% (HCK5) for horizontal cracks result in stronger δV_{LR}, but similar $\delta V_{LR}/\delta V_{LQ}$ ratios (Figure 6a). In a way, δV_{LR} and δV_{LQ} values increase with ε, and $\delta V_{LR}/\delta V_{LQ}$ ratios increase with AR for horizontal cracks.

For vertical cracks, increasing the AR from 10 (VCK6) to 30 (VCK9) with a fixed $\varepsilon = 2\%$ increases the *P*-wave radial anisotropy ϕ, but the *S*-wave radial anisotropy ξ is absent (i.e., $d\beta_V/d\beta_H = 1$). In the absence of ξ, the *P*-wave radial anisotropy ϕ alone still produces relatively large δV_{LQ} values and low $\delta V_{LR}/\delta V_{LQ}$ ratios, inconsistent with the observations (Figure 6a). With a fixed AR = 30, the effect of increasing crack densities from 0.5% (VCK7) to 1% (VCK8) to 2% (VCK9) for vertical cracks is similar to the effect in changing AR (Figure 6a). Since the alignment of vertical cracks leads to HTI with a slow symmetry axis along the horizontal axis, azimuthally averaged effective anisotropy ξ remains at 1, leading to relatively low $\delta V_{LR}/\delta V_{LQ}$ ratios.

Figure 6b summarizes the synthetic $\delta V_{LR}/\delta V_{LQ}$ ratios against ε, AR, and crack orientation in the presentation of crack geometry. Increasing the AR from 1 (the black circle) to 10 (the planar orange smarty) to 30 or 100 (the planar red smarty) with a fixed $\varepsilon = 2\%$ for horizontal cracks can enlarge the $\delta V_{LR}/\delta V_{LQ}$ ratio effectively, as indicated by the horizontal red arrow. Increasing the ε from 2% (the planar orange smarty) to 4% (the planar yellow

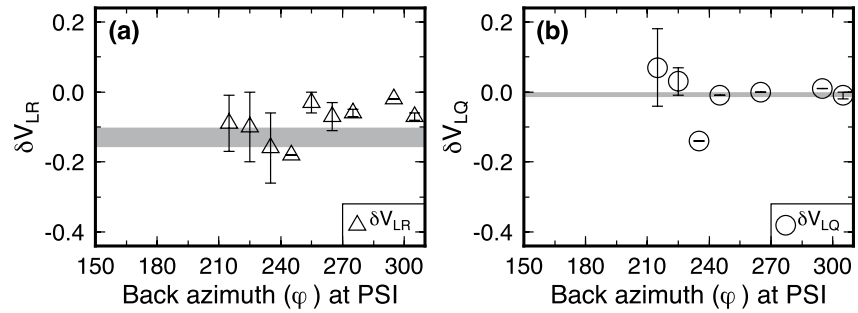

Figure 7. Back-azimuth dependence of (a) δV_{LR} and (b) δV_{LQ}. δV_{LR} or δV_{LQ} are averaged over 10° back-azimuth bins. The horizontal gray strip indicates the peak δV in Group 1 (Figure 3). The criteria for selecting the δV_{LR} and δV_{LQ} data from Group 1 are described in the text. We find minimal change in δV_{LR} or δV_{LQ} against back azimuth.

smarty) with a fixed AR = 10 for horizontal cracks produces a moderate $\delta V_{LR}/\delta V_{LQ}$ ratio, as indicated by the yellow arrow. For vertical cracks, increasing the AR from 10 (the vertical cyan smarty) to 30 (the vertical dark-green smarty) with a fixed $\varepsilon = 2\%$ produces large δV_{LR} and δV_{LQ} values and low $\delta V_{LR}/\delta V_{LQ}$ ratios, as indicated by the cyan arrow. Similarly, increasing the ε from 0.5% (the vertical light-green smarty) to 1% or 2% (the vertical dark-green smarty) with a fixed AR = 30 for vertical cracks also produces low $\delta V_{LR}/\delta V_{LQ}$ ratios, as indicated by the dark-green arrow. In summary, the observed large $\delta V_{LR}/\delta V_{LQ}$ ratios are consistent with horizontal cracks of $\varepsilon \approx 2.0\%$ and AR $\geq$ 10 confined to the uppermost 1 km of the crust, and they argue against predominant vertical cracks (i.e., scenario (I) and $d\alpha_H > d\alpha_V$).

6.2. Further Assessment of Changes in Azimuthal Anisotropy in HTI Media

We have demonstrated that the large $\delta V_{LR}/\delta V_{LQ}$ ratios reflect radial anisotropic changes due to an increase in ε for horizontal cracks of VTI media. On the other hand, near-surface temporal changes in azimuthal anisotropy have been documented in various tectonic regimes (Durand et al., 2011; Nakata & Snieder, 2012; Saade et al., 2017, 2019). While we have also shown that azimuthally averaged radial anisotropy from vertically aligned cracks of HTI media does not reproduce the observations of large $\delta V_{LR}/\delta V_{LQ}$ ratios, the azimuthal coverage of our data set is not perfect, and the validity of changes in azimuthal anisotropy in HTI media deserves further evaluation. Here we further examine if there is significant azimuthal anisotropy induced by vertically aligned cracks of HTI media. If the media were predominantly HTI, δV_{LR} from Rayleigh waves are dominated by a 2φ variation, whereas δV_{LQ} from Love waves are characterized by a 4φ variation (Montagner & Nataf, 1986; Tanimoto, 2004), where φ is the back azimuth.

To properly examine the azimuthal dependence of δV_{LR} and δV_{LQ}, it is important to minimize the effect of temporal change on these measurements. In the subsequent analysis, we select a subset of δV_{LR} and δV_{LQ} using the following criteria: (a) we restrict the time separation between the target and reference events in the range of 0.5–1.8 years. This allows a consistent sampling of the media in a coherent time interval while providing sufficient data and sampling in different back-azimuth swathes; (b) since δV_{LR} and δV_{LQ} immediately after great earthquakes are very sensitive to the event time, we select the target event of the REs between 0.1 and 0.6 years after the 2004 or 2005 great earthquakes. Figures 7a and 7b present the δV_{LR} and δV_{LQ} in 10° back-azimuth bins. In general, the magnitudes of δV_{LR} and δV_{LQ} in different back azimuthal bins are consistent with the values corresponding to the peak KDE in Figures 3a and 3b. Evidently, we do not observe notable 2φ azimuthal dependence in δV_{LR} (Figure 7a) nor 4φ azimuthal dependence in δV_{LQ} (Figure 7b), supporting our modeling of changes in radial anisotropy of VTI media near the surface.

Finally, as discussed in Y2020 and Section 5.3, to account for the observed δV_S, the velocity change in the lower crust is likely much smaller than that near the surface (Figure S12 in Supporting Information S1). While this study mostly emphasized changes in radial anisotropy near the surface, the estimated change of radial anisotropy near the surface is likely a lower bound if the effective reference media in the lower crust are not VTI. Regardless the nature of the effective anisotropy symmetry in the lower crust, its effect on our modeling result is likely minimal.

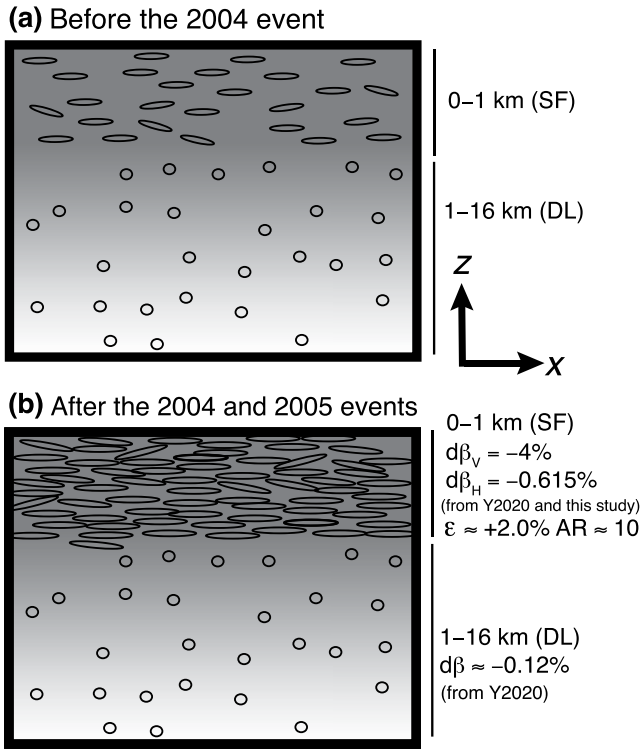

Figure 8. Inferred ε, crack geometry, crack orientation, and $d\beta_V$ and $d\beta_H$ in the near surface (0–1 km depth range, denoted as "SF," and indicated by the dark-gray hatched area) and 1–16 km depth range of the upper crust (deep layer, denoted as "DL" and indicated by the light-gray to white area) at two stages: (a) before the 2004 Great Sumatra Earthquake, and (b) after the 2004 Sumatra and 2005 Nias earthquakes. The SF zone in (a) possesses low ε values (indicated by the fewer number of cracks), whereas ε increases and the cracks are stretched horizontally (indicated by the higher number of the elongated cracks and AR ≈ 10 and $\varepsilon \approx +2.0\%$) in (b). Note that the inferred $d\beta_V$, $d\beta_H$, ε, and AR values in the SF zone are inferred from Y2020 and this study, whereas the $d\beta$ value in the DL is inferred from the HF δV_S discussed in Y2020.

6.3. Changes in Seismic Anisotropy After the Great Earthquakes in the Sumatra Subduction Zone

Figure 8 illustrates the schematic diagrams, highlighting the change in seismic anisotropy as a result of an increase in crack density after the 2004 and 2005 great earthquakes. In comparison to the state before the 2004 earthquake (dark-gray area, denoted "SF," Figure 8a), an increasing $\varepsilon \approx 2.0\%$ and AR ≥ 10 for horizontal cracks after the 2004 and 2005 earthquakes can produce $d\beta_V > d\beta_H$ and $d\alpha_V > d\alpha_H$ in the near surface (the SF zone, Figure 8b), thereby producing large $\delta V_{LR}/\delta V_{LQ}$ ratios. A stretch of the horizontal cracks is indicative of a change in radial anisotropy. A subtle $d\beta$ reduction of −0.12%, constrained by the subtle HF δV_S (Y2020), is below this strong near-surface $d\beta_V$ reduction (light-gray to white area, denoted "DL," Figure 8b).

As the *S*-wave polarized parallel to the plane of the cracks travels at a higher speed (Cochran et al., 2003; Crampin, 1981, 1984), our observed $\delta V_{LR} > \delta V_{LQ}$ (i.e., $d\beta_V > d\beta_H$) and the inferred horizontal cracks indeed agree with the inference of the higher *S*-wave velocity polarized in the direction parallel to the plane of horizontal cracks (i.e., $\beta_V < \beta_H$). However, planner cracks are typically aligned vertically when the least compressive stress σ_3 is horizontal, forming effective HTI media. In this case, one may expect to observe changes in azimuthal anisotropy near the surface after earthquakes (Durand et al., 2011; Saade et al., 2017). However, as discussed previously, our observations of large $\delta V_{LR}/\delta V_{LQ}$ ratios and the lack of azimuthal dependence of δV_{LR} or δV_{LQ} suggest predominant changes in radial anisotropy in VTI media. While we do not rule out that stress change after great earthquakes may reorient cracks and result in a change in azimuthal anisotropy, it probably occurs at a much lesser extent than the change in radial anisotropy as inferred by the observations of δV_{LR} and δV_{LQ}.

We suggest that the predominance of horizontally aligned cracks could be consistent with an overpressured, compressive environment near the subduction zone (i.e., $\sigma_V = \sigma_3$, where σ_V is the vertical stress and σ_3 is the least compressive stress). The overpressure state is defined when the pore-fluid pressure P_f is larger than hydrostatic pressure. It is commonly discussed in offshore environments (Dugan & Sheahan, 2012). The arrays of horizontal extension veins can be formed in metamorphic assemblages defining tensile overpressured compartments. Elevated pore-fluid pressure P_f has also been noted in the accretionary prism in the Sumatra forearc (Dean et al., 2010; McNeill & Henstock, 2014) as well as in other subduction zones (Saffer & Tobin, 2011).

As the rock tensile strength (T_O) is low (~1–10 MPa) for sedimentary rocks near the surface, it is conceivable that supralithostatic overpressure (i.e., $P_f = \sigma_3 + T_O$) under the condition $(\sigma_1 - \sigma_3)/T_O < 4$ results in extension fractures, forming sub-horizontal extension veins perpendicular to σ_3 (Figure 1 of Sibson, 2017). It is conceivable that, during the great earthquakes, rapid cyclic dynamic stresses from strong ground motions may compromise the rock strength (Bagde & Petros, 2005; Braunagel & Griffith, 2019; Erarslan & Williams, 2012), facilitating new horizontal extensional veins near the surface in the Sumatra forearc (Figure 8).

6.4. Enhanced Changes in Elastic Anisotropy as a Result of Repeating Loading-Unloading

Rock mechanics experiments demonstrated time-dependent anisotropy as a result of crack damage or subsequent closure (or recovery) (Meyer et al., 2021; Passelègue et al., 2018). In particular, Passelègue et al. (2018) monitored the elastic properties of Westerly granite during several cycles of loading and unloading, and discussed the evolution of strain, stress-induced elastic wave anisotropy associated with damage and healing. They demonstrated that the magnitude of damage-induced anisotropy increases after consecutive loading cycles. These

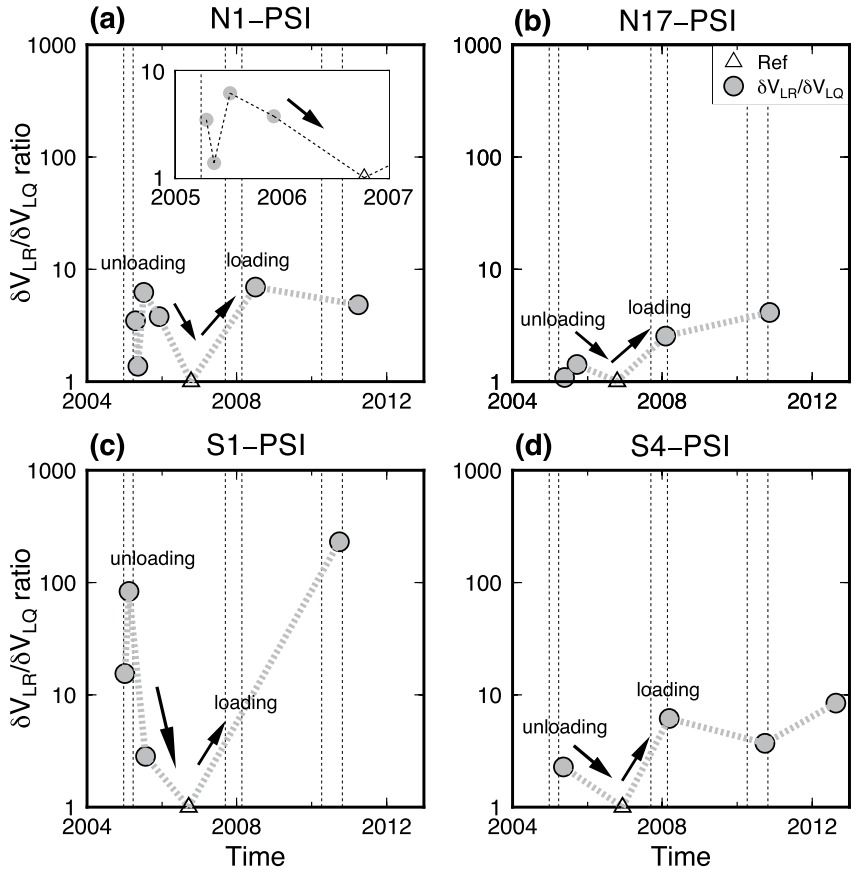

Figure 9. Temporal changes in near-surface radial anisotropy, as indicated by the $\delta V_{LR}/\delta V_{LQ}$ ratios (gray circles) for four RE sequences recorded at station PSI: (a) N1, (b) N17, (c) S1, and (d) S4, displayed over 2005–2013. The vertical dotted lines indicate the occurrence of the 2004, 2005, 2007, 2008, 2010 Banyak, and 2010 Mentawai earthquakes (Table S1), and the open triangle indicates the ratio at the reference event for each RE sequence, which is positioned at 1. An enlarged view is displayed in the inset in (a) to present better the decreasing $\delta V_{LR}/\delta V_{LQ}$ ratio during the 2005–2007 time period. Note that the $\delta V_{LR}/\delta V_{LQ}$ ratios of >80 in (c) are due to low δV_{LQ} <0.001%. Note that the decreasing radial anisotropy after the 2004 and 2005 great earthquakes is likely due to the closure of cracks (unloading), whereas sudden increasing radial anisotropy after late 2007 is due to loading induced by the ground motions of the 2007 and 2008 earthquakes.

experimental results apparently corroborate the notion of re-damaging inferred from our observations where the magnitude of δV_{LR} and radial anisotropy observed in Group 1 before the 2007 Bengkulu earthquakes are further enhanced in Group 2 after the 2007 sequence (Figures 3 and 9). Moreover, decreasing $\delta V_{LR}/\delta V_{LQ}$ ratio after the 2004 and 2005 great earthquakes is consistent with the reduction in the strength of elastic anisotropy due to the closure of cracks during the unloading stage (Figure 9).

7. Conclusions

This study examined temporal velocity changes from 20-s Rayleigh (δV_{LR}) and Love (δV_{LQ}) waves that were recorded at seismic station PSI using REs after the 2004 M_w 9.2 Sumatra Earthquake in the Sumatra Subduction Zone. Seismic observations revealed the following first-order patterns: (a) a δV_{LR} reduction of −0.16% was observed after the 2004 and 2005 M_w 8.6 Nias earthquakes, with an additional reduction of −0.25% observed after the 2007 M_w 8.4 and M_w 7.9 Bengkulu, and 2008 M_w 7.3 Simeulue earthquakes; (b) a weak δV_{LQ} reduction of −0.008% was observed after the 2004 and 2005 earthquakes, followed by an additional reduction of −0.027% after late 2007; and (c) the $\delta V_{LR}/\delta V_{LQ}$ ratio is ∼6. Two approaches were adopted to investigate the parameters that are sensitive to δV_{LR}, δV_{LQ}, and $\delta V_{LR}/\delta V_{LQ}$, including the Rayleigh-wave and Love-wave sensitivity kernels in isotropic and VTI media, and synthetic δV based on synthetic waveforms from the DSM in VTI media. The modeling result highlighted $d\beta_V \approx -4\%$ and $d\beta_H \approx -0.615\%$ confined to the uppermost 1 km of the crust, repro-

ducing the $\delta V_{LR}/\delta V_{LQ}$ ratio of 6. Furthermore, we show that the modeled $d\beta_V$ and $d\beta_H$ values can be reconciled by an increase in the crack density (ε) of 2.0% and a crack aspect ratio of $\geq$10 for fluid-filled horizontal cracks. Increasing horizontal cracks in the subduction zone forearc after great earthquakes may be facilitated in overpressured sediments. This study documented robust changes in radial anisotropy and presented the $\delta V_{LR}/\delta V_{LQ}$ ratio as a proxy to identifying/monitoring changes in near-surface radial anisotropy.

Data Availability Statement

The seismic data analyzed in this study were assembled from the Pacific 21 (PS) network, which was downloaded from the JAMSTEC data center, Japan (http://p21.jamstec.go.jp/top/) and IRIS DMC (http://service.iris.edu/fdsnws/dataselect/1/). The PDE event catalog was downloaded from ftp://hazards.cr.usgs.gov/NEICPDE/isf2.0. The DSM software package was downloaded from http://www-solid.eps.s.u-tokyo.ac.jp/~dsm/software/software.htm. The MSAT software package was downloaded from https://www1.gly.bris.ac.uk/MSAT/. The global CMT moment tensor was retrieved from https://www.globalcmt.org/.

Acknowledgments
The authors thank Editor Yehuda Ben-Zion and Associate Editor Nori Nakata for handling the manuscript and Jean-Paul Montagner and an anonymous reviewer for their constructive reviews and insightful comments. W.Y. wishes to thank input from Hsin-Ying Yang of University of Science and Technology of China, Li Zhao of Peking University, Fan-Chi Lin of University of Utah, and Cédric Legendre of Academia Sinica for discussions and suggestions. W.Y. was supported by the Institute of Earth Sciences, Academia Sinica, and grants MOST-104-2116-M-001-010-, MOST-107-2116-M-001-014-, and MOST-109-2116-M-001-027- from the Ministry of Science and Technology, Taiwan. T.R.A.S. acknowledges support from the Natural Environment Research Council (NE/P001378/1 and NE/T001372/1), United Kingdom.

References

Anderson, D. L. (1961). Elastic wave propagation in layered anisotropic media. *Journal of Geophysical Research*, *66*(9), 2953–2963. https://doi.org/10.1029/JZ066i009p02953

Anderson, D. L., Minster, B., & Cole, D. (1974). The effect of oriented cracks on seismic velocities. *Journal of Geophysical Research*, *79*(26), 4011–4015. https://doi.org/10.1029/JB079i026p04011

Babuska, V., & Cara, M. (1991). In G. Nolet (Ed.), *Seismic Anisotropy in the Earth* (p. 217). Kluwer Academic Publishers. https://doi.org/10.1007/978-94-011-3600-6

Bagde, M. N., & Petros, V. (2005). Fatigue properties of intact sandstone samples subjected to dynamic uniaxial cyclical loading. *International Journal of Rock Mechanics and Mining Sciences*, *42*(2), 237–250. https://doi.org/10.1016/j.ijrmms.2004.08.008

Bensen, G. D., Ritzwoller, M. H., Barmin, M. P., Levshin, A. L., Lin, F., Moschetti, M. P., et al. (2007). Processing seismic ambient noise data to obtain reliable broad-band surface wave dispersion measurements. *Geophysical Journal International*, *169*(3), 1239–1260. https://doi.org/10.1111/j.1365-246X.2007.03374.x

Bird, P. (2003). An updated digital model of plate boundaries. *Geochemistry, Geophysics, Geosystems*, *4*(3). https://doi.org/10.1029/2001GC000252

Braunagel, M. J., & Griffith, W. A. (2019). The effect of dynamic stress cycling on the compressive strength of rocks. *Geophysical Research Letters*, *46*(12), 6479–6486. https://doi.org/10.1029/2019GL082723

Brenguier, F., Campillo, M., Hadziioannou, C., Shapiro, N. M., Nadeau, R. M., & Larose, E. (2008). Postseismic relaxation along the San Andreas fault at Parkfield from continuous seismological observations. *Science*, *321*(5895), 1478–1481. https://doi.org/10.1126/science.1160943

Chen, L. W., Chen, Y. N., Gung, Y. C., Lee, J. C., & Liang, W. T. (2017). Strong near-surface seismic anisotropy of Taiwan revealed by coda interferometry. *Earth and Planetary Science Letters*, *475*, 224–230. https://doi.org/10.1016/j.epsl.2017.07.016

Chen, K. H., Furumura, T., & Rubinstein, J. (2015). Near-surface versus fault zone damage following the 1999 Chi-Chi earthquake: Observation and simulation of repeating earthquakes. *Journal of Geophysical Research: Solid Earth*, *120*, 2426–2445. https://doi.org/10.1002/2014JB011719

Chlieh, M., Avouac, J. P., Hjorleifsdottir, V., Song, T. R. A., Ji, C., Sieh, K., et al. (2007). Coseismic slip and afterslip of the great Mw 9.15 Sumatra–Andaman earthquake of 2004. *Bulletin of the Seismological Society of America*, *97*(1A), S152–S173. https://doi.org/10.1785/0120050631

Cochran, E. S., Vidale, J. E., & Li, Y. G. (2003). Near-fault anisotropy following the Hector Mine earthquake. *Journal of Geophysical Research*, *108*(B9), 2346. https://doi.org/10.1029/2002JB002352

Crampin, S. (1975). Distinctive particle motion of surface waves as a diagnostic of anisotropic layering. *Geophysical Journal of the Royal Astronomical Society*, *40*(2), 177–186. https://doi.org/10.1111/j.1365-246X.1975.tb07045.x

Crampin, S. (1981). A review of wave motion in anisotropic and cracked elastic-media. *Wave Motion*, *3*(4), 343–391. https://doi.org/10.1016/0165-2125(81)90026-3

Crampin, S. (1984). Effective anisotropic elastic constants for wave propagation through cracked solids. *Geophysical Journal of the Royal Astronomical Society*, *76*(1), 135–145. https://doi.org/10.1111/j.1365-246X.1984.tb05029.x

Crampin, S. (1987). Geological and industrial implications of extensive-dilatancy anisotropy. *Nature*, *328*, 491–496. https://doi.org/10.1038/328491a0

Crampin, S., Booth, D. C., Evans, R., Peacock, S., & Fletcher, J. B. (1990). Changes in shear wave splitting at Anza near the time of the North Palm Springs earthquake. *Journal of Geophysical Research*, *95*(B7), 11197–11212. https://doi.org/10.1029/JB095iB07p11197

Dean, S. M., McNeill, L. C., Henstock, T. J., Bull, J. M., Gulick, S. P. S., Austin, J. A., et al. (2010). Contrasting Décollement and Prism Properties over the Sumatra 2004−2005 Earthquake Rupture Boundary. *Science*, *329*(5988), 207–210. https://doi.org/10.1126/science.1189373

Dugan, B., & Sheahan, T. C. (2012). Offshore sediment overpressures of passive margins: Mechanisms, measurements, and models. *Reviews of Geophysics*, *50*(3). https://doi.org/10.1029/2011RG000379

Durand, S., Montagner, J. P., Roux, P., Brenguier, F., Nadeau, R. M., & Ricard, Y. (2011). Passive monitoring of anisotropy change associated with the Parkfield 2004 earthquake. *Geophysical Research Letters*, *38*(13). https://doi.org/10.1029/2011GL047875

Dziewonski, A. M., & Anderson, D. L. (1981). Preliminary reference Earth Model. *Physics of the Earth and Planetary Interiors*, *25*(4), 297–356. https://doi.org/10.1016/0031-9201(81)90046-7

Ekström, G., Nettles, M., & Dziewoński, A. M. (2012). The global CMT project 2004–2010: Centroid-moment tensors for 13,017 earthquakes. *Physics of the Earth and Planetary Interiors*, *200–201*, 1–9. https://doi.org/10.1016/j.pepi.2012.04.002

Erarslan, N., & Williams, D. J. (2012). Investigating the effect of cyclic loading on the indirect tensile strength of rocks. *Rock Mechanics and Rock Engineering*, *45*(3), 327–340. https://doi.org/10.1007/s00603-011-0209-7

Feng, L. J., Hill, E. M., Banerjee, P., Hermawan, I., Tsang, L. L. H., Natawidjaja, D. H., et al. (2015). A unified GPS-based earthquake catalog for the Sumatran plate boundary between 2002 and 2013. *Journal of Geophysical Research-Solid Earth*, *120*(5), 3566–3598. https://doi.org/10.1002/2014JB011661

Froment, B., Campillo, M., Chen, J. H., & Liu, Q. Y. (2013). Deformation at depth associated with the 12 May 2008 MW 7.9 Wenchuan earthquake from seismic ambient noise monitoring. *Geophysical Research Letters*, *40*(1), 78–82. https://doi.org/10.1029/2012GL053995

Hayes, G. P., Wald, D. J., & Johnson, R. L. (2012). Slab1.0: A three-dimensional model of global subduction zone geometries. *Journal of Geophysical Research*, *117*(B01302). https://doi.org/10.1029/2011JB008524

Hobiger, M., Wegler, U., Shiomi, K., & Nakahara, H. (2016). Coseismic and post-seismic velocity changes detected by Passive Image Interferometry: Comparison of one great and five strong earthquakes in Japan. *Geophysical Journal International*, *205*(2), 1053–1073. https://doi.org/10.1093/gji/ggw066

Hsu, Y. J., Simons, M., Avouac, J. P., Galetzka, J., Sieh, K., Chlieh, M., et al. (2006). Frictional afterslip following the 2005 Nias–Simeulue earthquake, Sumatra. *Science*, *312*(5782), 1921–1926. https://doi.org/10.1126/science.1126960

Huang, H., Yao, H. J., & van der Hilst, R. D. (2010). Radial anisotropy in the crust of SE Tibet and SW China from ambient noise interferometry. *Geophysical Research Letters*, *37*(L21310). https://doi.org/10.1029/2010GL044981

Huang, T. Y., Gung, Y., Kuo, B. Y., Chiao, L. Y., & Chen, Y. N. (2015). Layered deformation in the Taiwan orogen. *Science*, *349*, 720–723. https://doi.org/10.1126/science.aab1879

Hu, S. Q., Yao, H. J., & Huang, H. (2020). Direct surface wave radial anisotropy tomography in the crust of the Eastern Himalayan Syntaxis. *Journal of Geophysical Research: Solid Earth*, *125*(5). https://doi.org/10.1029/2019JB018257

Igarashi, T., & Kato, A. (2021). Evolution of aseismic slip rate along plate boundary faults before and after megathrust earthquakes. *Communications Earth and Environment*, *2*. https://doi.org/10.1038/s43247-021-00127-5

Ishii, M., Shearer, P. M., Houston, H., & Vidale, J. E. (2007). Teleseismic P wave imaging of the 26 December 2004 Sumatra−Andaman and 28 March 2005 Sumatra earthquake ruptures using the Hi-net array. *Journal of Geophysical Research*, *112*(B11307). https://doi.org/10.1029/2006JB004700

Jaxybulatov, K., Shapiro, N. M., Koulakov, I., Mordret, A., Landes, M., & Sens-Schönfelder, C. (2014). A large magmatic sill complex beneath the Toba caldera. *Science*, *346*(6209), 617–619. https://doi.org/10.1126/science.1258582

Jeng, J. Y., Askari, R., & Chatterjee, S. (2020). Correlation of near surface fractures with seismic radial anisotropy: An approach for near surface fracture identification. *Journal of Applied Geophysics*, *173*, 103925. https://doi.org/10.1016/j.jappgeo.2019.103925

Kawai, K., Takeuchi, N., & Geller, R. J. (2006). Complete synthetic seismograms up to 2 Hz for transversely isotropic spherically symmetric media. *Geophysical Journal International*, *164*(2), 411–424. https://doi.org/10.1111/j.1365-246X.2005.02829.x

Kawakatsu, H. (2016a). A new fifth parameter for transverse isotropy. *Geophysical Journal International*, *204*(1), 682–685. https://doi.org/10.1093/gji/ggv479

Kawakatsu, H. (2016b). A new fifth parameter for transverse isotropy II: Partial derivatives. *Geophysical Journal International*, *206*(1), 360–367. https://doi.org/10.1093/gji/ggw152

Kawakatsu, H., Montagner, J. P., & Song, T. R. A. (2015). On DLA's η. In G. R. Foulger, & M. Lustrino (Eds.), *The interdisciplinary Earth: A volume in Honor of Don L. Anderson* (pp. 33–38). GSA and AGU. https://doi.org/10.1130/2015.2514(03)

Konca, A. O., Avouac, J. P., Sladen, A., Meltzner, A. J., Sieh, K., Fang, P., et al. (2008). Partial rupture of a locked patch of the Sumatra megathrust during the 2007 earthquake sequence. *Nature*, *456*, 631–635. https://doi.org/10.1038/Nature07572

Konca, A. O., Hjorleifsdottir, V., Song, T. R. A., Avouac, J. P., Helmberger, D. V., Ji, C., et al. (2007). Rupture kinematics of the 2005 Mw 8.6 Nias–Simeulue earthquake from the joint inversion of seismic and geodetic data. *Bulletin of the Seismological Society of America*, *97*(1A), S307–S322. https://doi.org/10.1785/0120050632

Lange, D., Tilmann, F., Rietbrock, A., Collings, R., Natawidjaja, D. H., Suwargadi, B. W., et al. (2010). The fine structure of the subducted Investigator Fracture Zone in Western Sumatra as seen by local seismicity. *Earth and Planetary Science Letters*, *298*(1−2), 47–56. https://doi.org/10.1016/j.epsl.2010.07.020

Lin, F. C., Moschetti, M. P., & Ritzwoller, M. H. (2008). Surface wave tomography of the western United States from ambient seismic noise: Rayleigh and Love wave phase velocity maps. *Geophysical Journal International*, *173*(1), 281–298. https://doi.org/10.1111/j.1365-246X.2008.03720.x

Liu, Y., Zhang, H., Thurber, C., & Roecker, S. (2008). Shear wave anisotropy in the crust around the San Andreas Fault near Parkfield: Spatial and temporal analysis. *Geophysical Journal International*, *172*(3), 957–970. https://doi.org/10.1111/j.1365-246X.2007.03618.x

Maupin, V., & Cara, M. (1992). Love-Rayleigh wave incompatibility and possible deep upper mantle anisotropy in the Iberian Peninsula. *Pure and Applied Geophysics*, *138*(3), 429–444. https://doi.org/10.1007/BF00876881

McNeill, L. C., & Henstock, T. J. (2014). Forearc structure and morphology along the Sumatra Andaman subduction zone. *Tectonics*, *33*(2), 112–134. https://doi.org/10.1002/2012TC003264

Meyer, G. C., Brantut, N., Mitchell, T. M., Meredith, P. G., & Plümper, O. (2021). Time dependent mechanical crack closure as a potential rapid source of post-seismic wave speed recovery: Insights from experiments in Carrara Marble. *Journal of Geophysical Research: Solid Earth*, *126*(4). https://doi.org/10.1029/2020JB021301

Montagner, J. P., & Nataf, H. C. (1986). A simple method for inverting the azimuthal anisotropy of surface waves. *Journal of Geophysical Research*, *91*(B1), 511–520. https://doi.org/10.1029/JB091iB01p00511

Mordret, A., Shapiro, N. M., Singh, S., Roux, P., Montagner, J. P., & Barkved, O. I. (2013). Azimuthal anisotropy at Valhall: The Helmholtz equation approach. *Geophysical Research Letters*, *40*(11), 2636–2641. https://doi.org/10.1002/grl.50447

Moschetti, M. P., Ritzwoller, M. H., Lin, F., & Yang, Y. (2010). Seismic evidence for widespread western-US deep-crustal deformation caused by extension. *Nature*, *464*(7290), 885–889. https://doi.org/10.1038/nature08951

Naghavi, M., Hatami, M., Shirzad, T., & Rahimi, H. (2019). Radial anisotropy in the upper crust beneath the Tehran Basin and surrounding regions. *Pure and Applied Geophysics*, *176*(2), 787–800. https://doi.org/10.1007/s00024-018-1986-7

Nakata, N., & Snieder, R. (2011). Near-surface weakening in Japan after the 2011 Tohoku-Oki earthquake. *Geophysical Research Letters*, *38*(L17302). https://doi.org/10.1029/2011GL048800

Nakata, N., & Snieder, R. (2012). Time-lapse change in anisotropy in Japan's near surface after the 2011 Tohoku-Oki earthquake. *Geophysical Research Letters*, *39*(L11313). https://doi.org/10.1029/2012GL051979

Niu, F. L., Silver, P. G., Daley, T. M., Cheng, X., & Majer, E. L. (2008). Preseismic velocity changes observed from active source monitoring at the Parkfield SAFOD drill site. *Nature*, *454*(7201), 204–208. https://doi.org/10.1038/nature07111

O'Connell, R. J., & Budiansky, B. (1974). Seismic velocities in dry and saturated cracked solids. *Journal of Geophysical Research*, *79*(35), 5412–5426. https://doi.org/10.1029/JB079i035p05412

Parzen, E. (1962). On estimation of a probability density function and mode. *The Annals of Mathematical Statistics*, *33*(3), 1065–1076. https://doi.org/10.1214/aoms/1177704472

Passelègue, F. X., Pimienta, L., Faulkner, D., Schubnel, A., Fortin, J., & Guéguen, Y. (2018). Development and recovery of stress-induced elastic anisotropy during cyclic loading experiment on westerly granite. *Geophysical Research Letters*, *45*(16), 8156–8166. https://doi.org/10.1029/2018GL078434

Peng, Z. G., & Ben-Zion, Y. (2005). Spatiotemporal variations of crustal anisotropy from similar events in aftershocks of the 1999 M7.4 İzmit and M7.1 Düzce, Turkey, earthquake sequences. *Geophysical Journal International*, *160*(3), 1027–1043. https://doi.org/10.1111/j.1365-246X.2005.02569.x

Peng, Z. G., & Ben-Zion, Y. (2006). Temporal changes of shallow seismic velocity around the Karadere-Düzce branch of the North Anatolian fault and strong ground motion. *Pure and Applied Geophysics*, *163*, 567–600. https://doi.org/10.1007/s00024-005-0034-6

Poupinet, G., Ellsworth, W. L., & Frechet, J. (1984). Monitoring velocity variations in the crust using earthquake doublets: An application to the Calaveras Fault, California. *Journal of Geophysical Research*, *89*(B7), 5719–5731. https://doi.org/10.1029/JB089iB07p05719

Rivet, D., Campillo, M., Shapiro, N. M., Cruz-Atienza, V., Radiguet, M., Cotte, N., & Kostoglodov, V. (2011). Seismic evidence of nonlinear crustal deformation during a large slow slip event in Mexico. *Geophysical Research Letters*, *38*, L0830. https://doi.org/10.1029/2011GL047151

Rubinstein, J. L., Uchida, N., & Beroza, G. C. (2007). Seismic velocity reductions caused by the 2003 Tokachi-Oki earthquake. *Journal of Geophysical Research*, *112*(B05315). https://doi.org/10.1029/2006JB004440

Saade, M., Araragi, K., Montagner, J. P., Kaminski, E., Roux, P., Aoki, Y., & Brenguier, F. (2019). Evidence of reactivation of a hydrothermal system from seismic anisotropy changes. *Nature Communications*, *10*. https://doi.org/10.1038/s41467-019-13156-8

Saade, M., Montagner, J. P., Roux, P., Shiomi, K., Enescu, B., & Brenguier, F. (2017). Monitoring of seismic anisotropy at the time of the 2008 Iwate-Miyagi (Japan) earthquake. *Geophysical Journal International*, *211*(1), 483–497. https://doi.org/10.1093/gji/ggx321

Saffer, D. M., & Tobin, H. J. (2011). Hydrogeology and mechanics of subduction zone forearcs: Fluid flow and pore pressure. *Annual Review of Earth and Planetary Sciences*, *39*, 157–186. https://doi.org/10.1146/annurev-earth-040610-133408

Saito, M. (1988). DISPER80: A subroutine package for the calculation of seismic normal-mode solutions. In D. J. Doornbos (Ed.), *Seismological algorithms: Computational methods and computer programs* (pp. 293–319). Academic Press.

Savage, M. K., Peppin, W. A., & Vetter, U. R. (1990). Shear wave anisotropy and stress direction in and near Long Valley Caldera, California, 1979–1988. *Journal of Geophysical Research*, *95*(B7), 11165–11177. https://doi.org/10.1029/JB095iB07p11165

Sawazaki, K., Saito, T., & Shiomi, K. (2018). Shallow temporal changes in *S* wave velocity and polarization anisotropy associated with the 2016 Kumamoto earthquake sequence, Japan. *Journal of Geophysical Research-Solid Earth*, *123*(11), 9899–9913. https://doi.org/10.1029/2018JB016261

Shapiro, N. M., Ritzwoller, M. H., Molnar, P., & Levin, V. (2004). Thinning and flow of Tibetan crust constrained by seismic anisotropy. *Science*, *305*(5681), 233–236. https://doi.org/10.1126/science.1098276

Shirzad, T., Shomali, Z. H., Riahi, M. A., & Jarrahi, M. (2017). Near surface radial anisotropy in the Rigan area/SE Iran. *Tectonophysics*, *694*, 23–34. https://doi.org/10.1016/j.tecto.2016.11.036

Sibson, R. H. (2017). Tensile overpressure compartments on low-angle thrust faults. *Earth, Planets and Space*, *69*(113). https://doi.org/10.1186/s40623-017-0699-y

Snieder, R., Grêt, A., Douma, H., & Scales, J. (2002). Coda wave interferometry for estimating nonlinear behavior in seismic velocity. *Science*, *295*(5563), 2253–2255. https://doi.org/10.1126/science.1070015

Takagi, R., Okada, T., Nakahara, H., Umino, N., & Hasegawa, A. (2012). Coseismic velocity change in and around the focal region of the 2008 Iwate-Miyagi Nairiku earthquake. *Journal of Geophysical Research-Solid Earth*, *117*(B6). https://doi.org/10.1029/2012JB009252

Takeuchi, H., & Saito, M. (1972). Seismic surface waves. In B. A. Bolt (Ed.), *Methods in computational physics: Advances in research and applications*, *Seismology: Surface waves and Earth oscillations* (Vol. 11, pp. 217–295). Academic Press. https://doi.org/10.1016/B978-0-12-460811-5.50010-6

Tandon, G. P., & Weng, G. J. (1984). The effect of aspect ratio of inclusions on the elastic properties of unidirectionally aligned composites. *Polymer Composites*, *5*(4), 327–333. https://doi.org/10.1002/pc.750050413

Tanimoto, T. (2004). The azimuthal dependence of surface wave polarization in a slightly anisotropic medium. *Geophysical Journal International*, *156*(1), 73–78. https://doi.org/10.1111/j.1365-246X.2004.02130.x

Tomar, G., Shapiro, N. M., Mordret, A., Singh, S. C., & Montagner, J. P. (2017). Radial anisotropy in Valhall: Ambient noise-based studies of Scholte and Love waves. *Geophysical Journal International*, *208*(3), 1524–1539. https://doi.org/10.1093/gji/ggw480

Tsang, L. L. H., Hill, E. M., Barbot, S., Qiu, Q., Feng, L. J., Hermawan, I., et al. (2016). Afterslip following the 2007 Mw 8.4 Bengkulu earthquake in Sumatra loaded the 2010 Mw 7.8 Mentawai tsunami earthquake rupture zone. *Journal of Geophysical Research-Solid Earth*, *121*(12), 9034–9049. https://doi.org/10.1002/2016JB013432

Uchida, N., & Bürgmann, R. (2019). Repeating earthquakes. *Annual Review of Earth and Planetary Sciences*, *47*, 305–332. https://doi.org/10.1146/annurev-earth-053018-060119

Vidale, J. E., & Li, Y. G. (2003). Damage to the shallow Landers fault from the nearby Hector Mine earthquake. *Nature*, *421*, 524–526. https://doi.org/10.1038/nature01354

Wu, C. Q., Peng, Z. G., & Ben-Zion, Y. (2009). Non-linearity and temporal changes of fault zone site response associated with strong ground motion. *Geophysical Journal International*, *176*(1), 265–278. https://doi.org/10.1111/j.1365-246X.2008.04005.x

Xu, Z. J., & Song, X. (2009). Temporal changes of surface wave velocity associated with major Sumatra earthquakes from ambient noise correlation. *Proceedings of the National Academy of Sciences*, *106*(34), 14207–14212. https://doi.org/10.1073/pnas.0901164106

Yu, W., Lin, J. T., Su, J., Song, T. R. A., & Kang, C. C. (2020). *S* coda and Rayleigh waves from a decade of repeating earthquakes reveal discordant temporal velocity changes since the 2004 Sumatra earthquake. *Journal of Geophysical Research: Solid Earth*, *125*(7). https://doi.org/10.1029/2020JB019794

Yu, W., Song, T. R. A., & Silver, P. G. (2013a). Temporal velocity changes in the crust associated with the great Sumatra earthquakes. *Bulletin of the Seismological Society of America*, *103*(5), 2797–2809. https://doi.org/10.1785/0120120354

Yu, W., Song, T. R. A., & Silver, P. G. (2013b). Repeating aftershocks of the great 2004 Sumatra and 2005 Nias earthquakes. *Journal of Asian Earth Sciences*, *67*(68), 153–170. https://doi.org/10.1016/j.jseaes.2013.02.018

Zuo, Q. K., Tang, Y. C., Niu, F. L., Li, G. L., Chen, H. C., Tao, K., & Chen, B. (2018). Temporal variations of near-surface anisotropy induced by hydraulic fracturing at a Shale Play Site in southwest China. *Journal of Geophysical Research-Solid Earth*, *123*(9), 8032–8044. https://doi.org/10.1029/2018JB016037